

Melting Phase Relations of Simplified Carbonated Peridotite at 12–26 GPa in the Systems CaO–MgO–SiO₂–CO₂ and CaO–MgO–Al₂O₃–SiO₂–CO₂: Highly Calcic Magmas in the Transition Zone of the Earth

SHANTANU KESHAV^{1*}, GUDMUNDUR H. GUDFINNSSON² AND DEAN C. PRESNALL^{1,3,4}

¹BAYERISCHES GEOINSTITUT, UNIVERSITÄT BAYREUTH, BAYREUTH, GERMANY

²ICELAND GEOLOGICAL SURVEY, REYKJAVIK, ICELAND

³GEOSCIENCES, UNIVERSITY OF TEXAS AT DALLAS, RICHARDSON, TX 75083, USA

⁴GEOPHYSICAL LABORATORY, CARNEGIE INSTITUTION OF WASHINGTON, WASHINGTON DC 20015, USA

RECEIVED SEPTEMBER 7, 2009; ACCEPTED SEPTEMBER 16, 2011

Phase equilibrium data pertaining to melting of simplified carbonated peridotite in the systems CaO–MgO–SiO₂–CO₂ and CaO–MgO–Al₂O₃–SiO₂–CO₂ at pressures of 10–26 GPa, corresponding to ~300–750 km depths in the Earth, are presented. In both the studied systems, liquid compositions, with changing crystalline phase assemblage, are carbonatitic throughout the studied pressure range. In the system CMS–CO₂, melting phase relations are isobarically invariant; liquid is in equilibrium with forsterite + clinoenstatite + clinopyroxene + magnesite, forsterite + majorite + clinopyroxene + magnesite, wadsleyite + majorite + clinopyroxene + magnesite, ringwoodite + majorite + calcium-silicate perovskite + magnesite, magnesium-silicate perovskite + periclase + calcium-silicate perovskite + magnesite at 12, 14, 16, 20, and 26 GPa, respectively. In the system CMAS–CO₂, a phase assemblage consisting of forsterite + orthopyroxene + clinopyroxene + magnesite + garnet + melt from 10 to 14 GPa is isobarically invariant. However, owing to the disappearance of orthopyroxene at pressures greater than 14 GPa, from 16 and up to at least 26 GPa, the solidus of simplified carbonated peridotite spans a divariant surface in pressure–temperature space. The liquid coexists with wadsleyite + clinopyroxene + garnet + magnesite, ringwoodite + calcium-silicate

perovskite + garnet + magnesite, and magnesium-silicate perovskite + periclase + calcium-silicate perovskite + magnesite at 16, 20, and 26 GPa, respectively. A curious, and as yet unexplained, feature of our study is an abrupt drop in the solidus temperature between 14 and 16 GPa that causes a small amount of melting of carbonated mantle in the Transition Zone of the Earth. In the systems CMS–CO₂ and CMAS–CO₂ liquid compositions at 16 and 20 GPa are highly calcic bona fide carbonatites; however, these liquids revert to being magnesian-carbonatites at 10–14 and 26 GPa. In the system CMS–CO₂, at 16 GPa we locate an isobaric invariant point consisting of wadsleyite + clinopyroxene + anhydrous B + magnesite + melt. The presence of anhydrous B at 16 GPa and 1475°C is interesting, as it lies outside the composition space of the mantle peridotite analog we have studied. However, despite the presence of two highly magnesian silicate crystalline phases, wadsleyite and anhydrous B, at 16 GPa and 1475°C, the liquid composition remains calcic with molar Ca-number [Ca/(Ca + Mg) × 100] of about 63. The melting reactions at 16 and 20 GPa (with or without anhydrous B) show that lime-bearing crystalline silicates play a fairly large part in generating and controlling the composition of the liquids. At 16 GPa, in the system CMS–CO₂, we also report an experimental run at 1575°C, in which liquid coexists

*Corresponding author. Present address: Geosciences Montpellier, University of Montpellier 2, CNRS & UMR 5243, Montpellier, France. Telephone: +33-467-14-3947. E-mail: keshav@gm.univ-montp2.fr

with only wadsleyite and majorite. The liquid composition is less calcic (*Ca*-number 54) than that for other runs at lower temperatures, but is still more calcic than liquids at 10–14 and 26 GPa in both the studied systems. At present, the likely cause for these changes in the reported phase relations is not known. For normally assumed mantle temperatures, melting in the Transition Zone of the Earth, owing to the presence of carbonate, is probably unavoidable. The depth range of the drop in the carbonated peridotite solidus closely matches that of commonly observed low seismic velocities at ~400–600 km depth in the Earth.

KEY WORDS: *solidus; melting; peridotite; carbonatites; carbonate*

INTRODUCTION

The presence of carbonatites, magmas that have almost no silica and are dominantly composed of CaO, MgO, and CO₂, in the sub-oceanic mantle has been inferred on the basis of the geochemistry of mid-ocean ridge (McKenzie, 1984; Presnall *et al.*, 2002; Presnall & Gudfinnsson, 2008) and ocean-island basalts (Dixon *et al.*, 2008; Sisson *et al.*, 2009). Coupled with experimental petrology (Eggler, 1976; Wyllie & Lee, 1998, and references therein), indications that such low-silica magmas are perhaps common in the sub-oceanic mantle (or in general, perhaps in the Earth) have also come from studies of mantle xenoliths recovered in ocean-island basalt localities (Hauri *et al.*, 1993; Keshav & Sen, 2003). The influence of carbon dioxide in mantle melting at mid-ocean ridges has recently been reported in geophysical studies (Sohn *et al.*, 2008; Clague *et al.*, 2009). Diamonds from the continental mantle contain carbonatitic melts or fluids (Schrauder & Navon, 1994; Schrauder *et al.*, 1996; Klein-BenDavid *et al.*, 2004, 2006, 2007; Tomlinson *et al.*, 2006, 2009). On the basis of the trace element patterns of certain silicate inclusions, the antiquity of such diamonds has been questioned (Shimizu & Sobolev, 1995; Taylor *et al.*, 2003). Such patterns, it has been suggested, can develop when carbonatite-like fluids or melts interact with solid silicates in diamonds (Taylor *et al.*, 2003).

Diamonds containing Transition Zone and lower mantle assemblages are also transported to the Earth's surface by violent kimberlite eruptions (Stachel *et al.*, 2000; Kaminsky *et al.*, 2001; Stachel, 2001; Brenker *et al.*, 2002; Pearson *et al.*, 2003) that appear to be related to carbonatitic activity in the source region of these very deep magmas. In at least some diamonds of purported Transition Zone and lower mantle origin, crystalline carbonate has also been recovered as an inclusion (Brenker *et al.*, 2007, and references therein), suggesting that carbonate in our planet perhaps extends deeper than previously thought. Silicate inclusions in some cratonic diamonds are interpreted to have grown from carbonatitic melts (Keshav *et al.*, 2006; Armstrong *et al.*, 2007, 2008; Walter *et al.*, 2008), indicating that not only solid carbonate

but also carbonatitic liquids might be generated at moderately great depths in the Earth, and some natural specimens seemingly have documented evidence of such melting. All these observations have consequences for our understanding of carbonate-assisted melting processes at various depths in the Earth, the influence of this melting on the overall petrology of the mantle, the stability of crystalline carbonate, the relationship (if any) of carbonatitic liquids with other magma types, and eventually the recognition, in mantle specimens, of geochemical signatures that have been brought about by carbonatitic magmas.

Previously, in an effort to understand better the genesis of carbonatites and kimberlites, and the stability of crystalline carbonate, first Canil & Scarfe (1990) and later Dalton & Presnall (1998) reported melting phase relations of simplified carbonated peridotite at and above 3–4 GPa. In this respect, the results of these two studies deserve some attention. Whereas Canil & Scarfe (1990) in the systems CaO–MgO–SiO₂–CO₂ (CMS–CO₂) and CaO–MgO–Al₂O₃–SiO₂–CO₂ (CMAS–CO₂) reported that near-solidus liquids from ~4 to 12 GPa were similar to erupted kimberlites, Dalton & Presnall (1998) in the system CMAS–CO₂ continued to observe near-solidus, experimental liquids at 3–7 GPa that bore similarities to calcio- and magnesio-carbonatites. To generate a large amount of liquid at the initiation of melting, while maintaining an assemblage consisting of forsterite–orthopyroxene–clinopyroxene–garnet–crystalline carbonate–liquid, Dalton & Presnall (1998) ‘tailored’ their starting compositions. The above-mentioned phase assemblage is univariant in pressure–temperature (*P–T*) space. As has been the tradition, and also observed by Luth (1999), this technique allows one to determine liquid compositions, and as an outcome, solidus temperatures, with much greater confidence than where the melt fraction at the solidus is exceedingly small (for instance, Canil & Scarfe, 1990). This philosophy, as Luth (1999) pointed out, might have led to the contrasting solidus temperatures, because in the study by Canil & Scarfe (1990), the experiments generated a small amount of melt near the solidus, and consequently its detection in polished sections, and a good microprobe analysis, is perhaps made difficult. However, in both the studies by Canil & Scarfe (1990) and Dalton & Presnall (1998), above about 4.5 GPa, magnesite was the stable crystalline carbonate phase at the solidus. The observation that the liquid composition stays carbonatitic up to about 7 GPa, even when the stable carbonate phase switched from dolomite to magnesite along the solidus of carbonated peridotite (Dalton & Presnall, 1998), is in contrast to previous suggestions (Brey *et al.*, 1983; Katsura & Ito, 1990), where an increase in the MgO concentration of the first liquid at the solidus, at the onset of transformation of dolomite to magnesite, was predicted to happen.

In multicomponent (high-variance) systems, Hirschmann & Dasgupta (2007), using published liquid compositions in the system CMAS–CO₂ (Dalton & Presnall, 1998) and data from the Wallace & Green (1988) experimental study, have attempted to clarify what initial melts might look like at 6–6 GPa in multicomponent carbonated peridotite, and as a consequence, the solidus temperatures of such carbonated peridotite. Most recently, Ghosh *et al.* (2009) have published melting phase relations at pressures of 10–20 GPa in alkalic, multicomponent carbonated peridotite. The solidus curve of carbonated peridotite that Ghosh *et al.* (2009) reported has a positive slope in the pressure range 9–13 GPa, but at higher pressures, up to 20 GPa, it is essentially flat.

Litasov & Ohtani (2009), in their study on carbonated peridotite at 10–32 GPa, worked with the low-variance system CMAS–Na₂O–CO₂ (CMASN–CO₂). Given the nature of these experiments at such elevated pressures, especially in chemically simple systems, their results are a valuable contribution. The solidus curve reported by Litasov & Ohtani (2009) rises gently in P – T space from about 1400°C at 10 GPa to roughly 1700°C at 25 GPa, and shows signs of flattening up to the highest pressure investigated of 32 GPa. Liquid compositions, as expected, are sodic, reaching values as high as about 5 wt %. Additionally, on the basis of mass balance, Litasov & Ohtani suggested that solid CO₂ (carbon dioxide) might be a stable phase above about 27 GPa, an observation that has consequences for how carbon dioxide and its various forms (solid, liquid, vapour) are stored at such depths in the Earth.

Ghosh *et al.* (2009) and Litasov & Ohtani (2009) reported very different solidus curves, although to some extent the liquid compositions partially overlap in these two studies. Compared with the curves of Ghosh *et al.* (2009) and Litasov & Ohtani (2009), the solidus curve of multicomponent, carbonated peridotite in the pressure range 10–23 GPa, as shown by Rohrbach & Schmidt (2011), is also flat in P – T space.

Here we report the results of an experimental study aimed at clarifying the melting phase relations of carbonated peridotite at pressures of 12–26 GPa. This pressure range corresponds to depths of ~350–750 km in the Earth. Some important starting points for discussion are as follows: (1) What are the solidus temperatures? (2) What is the topology of the melting curve in P – T space? (3) What are the liquid compositions in equilibrium with a defined crystalline phase assemblage? (4) Do liquid compositions in equilibrium with a particular phase assemblage at the solidus become ‘kimberlitic’, as suggested in at least two previous studies (Brey *et al.*, 1983; Canil & Scarfe, 1990)? To address these issues in a tractable way we have focused on simplified carbonated peridotite in the systems CaO–MgO–SiO₂–CO₂ (CMS–CO₂) and the

slightly more complex CaO–MgO–Al₂O₃–SiO₂–CO₂ (CMAS–CO₂). We have considered that part of the composition space in these two systems that is analogous to the natural, carbonate-bearing mantle system with a peridotitic bulk composition. At a fixed pressure in these systems, the studied phase relations involving all the required phases at the solidus are either isobarically invariant or univariant. This approach also means that as long as all the phases at the solidus are present in the experimental runs, the choice of starting composition does not affect the phase compositions, and the bulk compositions can be adjusted so as to maximize the amount of liquid (or any other phase) in the experiments. Subsequently, the phase equilibrium data can be used to model very small degrees of melting in a portion of the mantle with the same phase assemblage. Therefore, by studying the systems CMS–CO₂ and CMAS–CO₂, experimental liquids that are analogous to very small degree mantle melts can be readily analyzed by electron microprobe and solidus temperatures as a function of pressure can be rigorously determined. Increasing complexity (in terms of chemical components) can subsequently be added to the above systems, as has been done in the past (e.g. Walter & Presnall, 1994; Sisson *et al.*, 1997; Gudfinnsson *et al.*, 2007, 2008; Keshav & Gudfinnsson, 2009). This is a huge advantage over experiments that employ multicomponent (natural) starting compositions to determine the solidus, in which the temperature of initial melting is difficult to detect, the solidus is a function of the bulk CO₂ concentration, and the initial melts are almost impossible to analyze because of their small volume (Wallace & Green, 1988; Falloon & Green, 1989; but also see Hirschmann & Dasgupta, 2007).

EXPERIMENTAL AND ANALYTICAL DETAILS

Starting mixtures

Starting compositions, which were mixtures of finely ground silicate glasses and magnesite, were made following the procedures outlined in previous studies (Dalton & Presnall, 1998; Gudfinnsson & Presnall, 2005; Keshav *et al.*, 2005). The compositions of the starting mixtures are provided in Tables 1 and 2. In Table 2, an electron microprobe analysis (wt %) of bulk composition CMS–CO₂-2-A is provided. This experimental charge was treated in a 10/5-type (see below) pressure cell at 20 GPa and 1950°C for 1.5 h, using identical procedures to those described below. Analyses are an average of 20 scans performed using a probe beam diameter of 5 µm. The overlap between the nominal and analysed bulk composition is fairly good, confirming the homogeneity of the starting mixtures used in this work. The amount of CO₂ in the bulk melt was calculated by difference.

Table 1: Nominal composition of starting mixtures in the systems CMS-CO₂ and CMAS-CO₂ used in the present study (by weight)

Mixture	CaO	MgO	Al ₂ O ₃	SiO ₂	CO ₂ *
CMS-CO ₂ -1	16.97	33.91	-	27.71	21.41
CMS-CO ₂ -3-A	21.63	30.76	-	23.22	24.39
CMS-CO ₂ -3-B	21.48	30.61	-	24.01	23.90
CMS-CO ₂ -2-A	29.15	24.54	-	20.79	25.52
CMS-CO ₂ -2-B	29.60	25.10	-	20.87	24.43
CMS-CO ₂ -6	15.57	33.97	-	33.21	17.25
CMS-CO ₂ -7	14.95	32.78	-	34.70	17.57
CMAS-CO ₂ -21-A	12.37	36.70	1.64	27.67	21.63
CMAS-CO ₂ -21-B	11.00	35.95	2.04	30.41	20.60
CMAS-CO ₂ -23-A	11.11	39.93	0.24	27.51	21.21
CMAS-CO ₂ -23-B	9.63	38.09	1.28	31.12	19.90
CMAS-CO ₂ -19-A	13.66	32.78	1.77	31.58	21.10
CMAS-CO ₂ -19	12.20	34.51	1.71	30.49	21.09
CMAS-CO ₂ -14-A	20.54	28.34	2.51	28.77	19.84
CMAS-CO ₂ -14-B	21.95	27.24	2.57	24.94	23.30
CMAS-CO ₂ -15-A	25.15	25.42	1.53	29.44	18.46
CMAS-CO ₂ -15-B	25.14	26.26	1.75	28.40	18.45
CMAS-CO ₂ -16-A	18.90	34.04	1.15	23.59	22.32
CMAS-CO ₂ -16-B	19.33	31.62	1.14	24.34	23.57

*By difference.

Experimental procedures and analytical methods

All the experiments were performed at the Bayerisches Geoinstitut (BGI), Germany, using a multianvil apparatus. The device used has a maximum thrust of 1200 ton (Sumitomo 1200). The experiments were performed using Cr₂O₃-doped MgO pressure cells at 10–14 GPa with an edge length of 14 mm, and at 16, 20, and 26 GPa with an edge length of 10 mm. Second-stage tungsten carbide anvils (32 mm edge length) with 8 mm (Toshiba F grade), 5 mm (Toshiba F grade), and 4 mm (Widia F grade) truncated edge lengths were employed in experiments at 10, 12, and 14 GPa, 14, 16 and 20 GPa, and 26 GPa, respectively. Experiments at 14 GPa were also performed using pressure cells with an edge length of 10 mm and tungsten carbide anvils with 5 mm truncation. Pyrophyllite was used as gasket material in all the experiments. All the pressure cells used have similar internal configurations. They consist of zirconia thermal insulators, dense four-bore alumina sleeves for thermocouples, and soft magnesia and alumina inserts. Cells with 14 and 10 mm edge length have stepped and straight lanthanum chromate (LaCrO₃) heaters, respectively. In all pressure cells, molybdenum (Mo) rings

Table 2: Electron microprobe analyses (wt %) of starting mixture CMS-CO₂-2-A

Oxide	CMS-CO ₂ -2-A
CaO	28.58 (0.12)
MgO	23.58 (0.94)
SiO ₂	22.41 (0.44)
CO ₂	25.41*

*By difference.

The mixture CMS-CO₂-2-A was melted in a 10/5 pressure cell at 20 GPa and 1950°C for 1.5 h, following the procedures described in the text. Analyses are an average of 20 scans performed using an electron microprobe beam diameter of 5 µm. The overlap between the nominal (prepared from oxides or carbonate) and analysed bulk composition is fairly good, confirming the homogeneity of the starting mixtures used in this work. The amount of CO₂ in the bulk melt was calculated by difference.

on either end of the heaters serve as electric contacts with the anvils. For the experiments, ~0.5 mg of a starting mix was loaded into a Pt capsule (1.2 or 1.6 mm outer diameter; 1.1–2.0 mm final length) that had previously been annealed in air at 1000°C, sealed at one end by arc welding, boiled in dilute HCl (30 min), ultrasonically cleaned in ethanol (10 min), and fired again in air at 1000°C for 10 min. Before assembling the pressure cell, the loaded capsule was again dried in air at 175–200°C for over 14 h.

Run temperature was measured using type D (W₇₅Re₂₅/W₉₇Re₃) thermocouple wires (0.15 or 0.13 mm thick; Omega[®]) in contact with the Pt capsule. Temperatures reported are thermocouple readings; the effect of pressure on the thermocouple e.m.f. was ignored. Temperature was controlled to within ±2°C of the target temperature using a Eurotherm controller. To ensure anhydrous conditions during the experiments, all the cell parts (except Mo electrodes and capsules) were fired in air at 1000°C in a box furnace for 1 h. After construction and before an experiment, the entire cell was kept dry in an oven at 175°C. After each run, the Pt capsule was recovered from the cell, mounted longitudinally in epoxy, and ground and polished for optical and electron microprobe examination. After termination of an experiment, the thermocouple junction was always confirmed as being in direct contact with the capsule. All the experimental runs were polished under water-absent conditions, and charges also had to be frequently (3–4 times) vacuum-impregnated with resin.

Because of the lack of any suitable temperature monitor at these elevated pressure and temperature conditions, attempts were not made to calibrate the temperature distribution in the sample capsules employed in the present set of experiments. Instead, on the basis of the experimental

results reported here, we infer that the temperature reproducibility is of the order of about ± 25 – 30°C . This conclusion is based on the following: (1) the Pt capsules used in the experiments were very small (1–2 mm long; in most cases 1–1.5 mm long); (2) the dimensions of a particular experimental charge in the capsules, in general, did not exceed $\sim 500\ \mu\text{m} \times 500\ \mu\text{m}$, and therefore the charge was surrounded with a relatively large volume of metal, which tends to even out the temperature in the capsule; (3) more significantly, melt compositions were uniform from spot to spot (reflected in the uncertainty cited; see Tables 3 and 4). The overlap in the electron microprobe analyses of interstitial melt pockets, and segregated pools of melt suggests minimal temperature gradients in the metal capsules. The same is true of the crystalline phase compositions, analysed either near the melt–crystal interface or well inside the crystalline portion (in physical contact with interstitial melt pockets) of the experimental charge. Additionally, between 14 and 16 GPa, we can clearly distinguish the distinct nature of melts produced in equilibrium with their respective crystalline phase assemblage. Therefore, on the basis of all of the above, we are fairly sure in stating that the temperature uncertainty in the sample capsules is roughly ± 25 – 30°C , and is reproducible.

High-temperature (1200–1600°C) calibrations for the pressure cells employed in this study are based on previous experiments carried out using the Sumitomo 1200 at Bayerisches Geoinstitut. These determinations have been reported in various publications (Canil, 1994; Frost *et al.*, 2001; Keppler & Frost, 2005). Briefly, these fixed pressure points have employed coesite–stishovite, forsterite–wadsleyite, wadsleyite–ringwoodite, and the dissociation of ringwoodite to magnesium-silicate perovskite and periclase phase boundaries. The interested reader is referred to the above-mentioned publications for further details.

The compositions of the crystalline phases and melt were determined by wavelength-dispersive electron microprobe analyser (five-spectrometer JEOLJXA-8900 Superprobe at BGI) with an accelerating voltage of 15 kV and 15 nA probe current (at the Faraday cup). Melt was analyzed using a beam diameter of 5–10 μm . In some experiments, despite several sessions of gentle polishing and vacuum impregnation, the surface of the exposed charge was still rough. Therefore, in such cases, more than 15 melt areas were analyzed with the electron microprobe. The beam diameter was 1–2 μm for crystalline phases, and all the analyses were performed in a fixed spot mode. Analyses were reduced using the ZAF correction scheme, and the amount of CO_2 dissolved in the melt and crystalline carbonate was calculated by difference. All four oxides were measured using a combination of forsterite, diopside, pyrope, and enstatite standards. For further details, the interested reader is referred to the study by Gudfinnsson & Presnall (2005).

DESCRIPTION OF EXPERIMENTAL CHARGES

In the experiments reported here, melt does not occur as glass, but as an intergrowth of silicates and carbonates (hereafter, quench refers to quenched melt = liquid). Melt is mainly present as separate pools (~ 300 – $600\ \mu\text{m}$ long by ~ 200 – $300\ \mu\text{m}$ wide), but interstitial melt pockets (~ 2 – $30\ \mu\text{m}$ across) are also seen. After quantitative analysis, areas of quench crystals always show some beam damage. The crystalline carbonate phase, which is always magnesite with a limited amount of calcite solid solution, tends to occur uniformly throughout the charge, and in contact with large quench pools. Magnesite also occurs in physical contact with pockets of interstitial melt. In backscatter electron (BSE) images, it is comparatively the darkest phase. In some runs, crystalline carbonate was also seen to occur as a dark band separated from the main quench melt pool, but in such cases, smaller quench pockets (10–20 μm) were always observed to be in contact with the carbonate.

In the systems CMS-CO_2 and CMAS-CO_2 , forsterite (Figs 1 and 2), wadsleyite (Fig. 3), and ringwoodite (Fig. 4) occur at 10, 12, 14, 16, and 20 GPa, and range from about 10 to 70 μm across. Under the electron microprobe beam, forsterite, wadsleyite, and ringwoodite emit slightly purple, bright green, and dark bluish-green fluorescence colors, respectively. These phases are invariably seen to be in contact with quenched melt. Enstatite occurs in experiments performed at 10 and 12 GPa (Fig. 1). In backscatter images, it is medium grey in color, appears to be anhedral to subhedral in outline, tends to occur in clusters, and ranges between 7 and 20 μm in diameter. The brightest phases in all the experiments, as observed in backscatter images, are either clinopyroxene or calcium perovskite. Clinopyroxene, which is present at 10, 12 (Fig. 1), 14 (Fig. 2), and 16 GPa (Fig. 3), occurs as equant-shaped grains. It ranges between ~ 10 and 40 μm across, is always in contact with either large quench pools or smaller melt pockets, and also occurs uniformly throughout the charge. It emits pale blue fluorescence under the electron microprobe beam. In places, it occurs as an inclusion in either forsterite or wadsleyite.

Calcium perovskite, which is present in experiments at 20 (Fig. 4) and 26 GPa (Fig. 5), lacks textural homogeneity and crystal outlines, and dominantly occurs as small (~ 10 – $30\ \mu\text{m}$), amorphous looking masses. Like other phases, it is in contact with quench pools or pockets. It almost always exhibits evidence of beam damage under the electron microprobe beam, and it appears that the amorphous nature is related to its transformation during decompression (Liu & Ringwood, 1975; Canil, 1994). Majorite occurs in the experiments at 14 (Fig. 2), 16 (Fig. 3), and 20 GPa (Fig. 4). It can be hard to identify, both under reflected light or in backscatter images.

Table 3: Experimental details, run products, and electron microprobe analyses (in wt %) of crystalline phases and quenched melts at the solidus of simplified carbonated peridotite in the system CMS-CO₂

Experiment	CaO	MgO	SiO ₂	CO ₂	Sum	Ca-no. ¹
<i>1 (CMS-CO₂-6);² 12 GPa, 1525° C, 7 h³</i>						
Forsterite (11) ⁴	0.31 (0.13)	56.69 (0.49)	43.10 (0.40)		100.10	
Cpx (19)	23.26 (0.78)	21.38 (0.74)	54.93 (0.67)		99.57	
Mag (14)	1.79 (0.66)	40.53 (0.51)	-	57.68 ⁵	100.00	3.05
<i>2 (CMS-CO₂-6); 12 GPa, 1550° C, 5 h³</i>						
Forsterite (7) ⁴	0.23 (0.08)	56.13 (0.20)	42.71 (0.31)		99.07	
Cpx (9)	23.54 (0.59)	20.46 (0.68)	56.47 (0.41)		100.47	
Mag (11)	4.55 (0.44)	37.64 (0.29)	-	57.81	100.00	8.03
<i>3 (CMS-CO₂-6); 12 GPa, 1575° C, 5 h</i>						
Forsterite (12) (19) ⁶	0.14 (0.01)	57.05 (0.12)	42.60 (0.17)		99.80	
Cpx (15) (15)	15.65 (0.86)	26.75 (0.75)	57.13 (0.23)		99.54	
En (11) (18)	2.29 (0.34)	38.21 (0.38)	58.89 (0.17)		99.39	
Melt (30) (48)	22.56 (1.22)	24.06 (0.90)	15.32 (1.27)	38.05	100.00	40.11
<i>4 (CMS-CO₂-7); 14 GPa, 1625° C, 5 h</i>						
Forsterite (13) (18)	0.20 (0.01)	57.12 (0.18)	42.24 (0.18)		99.55	
Cpx (12) (41)	21.12 (1.18)	22.37 (0.95)	55.69 (0.21)		99.17	
Maj (11) (2)	2.83 (0.51)	38.77 (0.49)	57.66 (0.27)		99.26	
Mag (10) (16)	2.76 (0.26)	39.39 (0.24)	-	57.84	100.00	4.76
Melt (30) (23)	24.80 (4.17)	26.62 (4.56)	12.76 (5.06)	35.81	100.00	39.95
<i>5 (CMS-CO₂-3-A); 16 GPa, 1475° C, 8 h</i>						
Wad (11) (20)	0.27 (0.11)	56.87 (0.51)	42.39 (0.44)		99.53	
Cpx (16) (22)	24.79 (0.79)	19.17 (0.81)	56.17 (0.55)		100.13	
AnhyB (9) (5)	0.21 (0.15)	65.29 (0.63)	35.11 (0.70)		100.61	
Mag (13) (17)	2.19 (0.58)	39.11 (0.76)	-	58.70	100.00	3.84
Melt (27) (36)	39.47 (2.27)	16.11 (1.86)	3.27 (1.23)	41.15	100.00	63.63
<i>6 (CMS-CO₂-3-A); 16 GPa, 1510° C, 5 h</i>						
Wad (9) (25)	0.35 (0.10)	57.19 (0.23)	42.61 (0.31)		100.15	
Cpx (9) (19)	21.61 (0.83)	22.10 (0.73)	55.99 (0.51)		99.70	
Mag (10) (11)	2.83 (0.22)	39.11 (0.19)	-	58.06	100.00	4.91
Melt (30) (45)	38.19 (1.23)	17.45 (0.83)	4.40 (1.09)	39.96	100.00	61.47
<i>7 (CMS-CO₂-3-B); 16 GPa, 1525° C, 5 h</i>						
Wad (13) (27)	0.27 (0.03)	56.93 (0.16)	42.31 (0.14)		99.51	
Cpx (10) (2)	21.15 (0.99)	22.51 (0.89)	56.23 (0.34)		99.89	
Maj (10) (12)	5.94 (0.12)	33.79 (0.24)	59.89 (0.25)		99.62	
Melt (30) (59)	34.27 (0.91)	18.01 (0.78)	7.25 (1.49)	40.47	100.00	59.21
<i>8 (CMS-CO₂-3-B); 16 GPa, 1575° C, 5 h</i>						
Wad (9) (27)	0.29 (0.11)	57.34 (0.30)	43.05 (0.23)		100.68	
Maj (10) (12)	6.20 (0.28)	34.27 (0.55)	58.61 (0.49)		99.08	
Melt (45) (61)	31.79 (1.04)	19.11 (1.33)	9.64 (2.31)	39.46	100.00	54.30
<i>9 (CMS-CO₂-2-A); 20 GPa, 1700° C, 4 h</i>						
Rw (12) (19)	0.11 (0.02)	57.30 (0.23)	42.23 (0.20)		99.64	
Capv (7) (21)	47.07 (0.98)	0.51 (0.23)	50.71 (1.19)		98.29	
Mag (10) (12)	2.69 (0.47)	40.01 (0.26)	-	57.30	100.00	4.58
Melt (35) (48)	39.13 (0.28)	18.22 (0.37)	4.23 (0.82)	38.42	100.00	62.03
<i>10 (CMS-CO₂-2-B); 20 GPa, 1750° C, 3 h</i>						
Rw (9) (20)	0.31 (0.12)	56.89 (0.39)	43.01 (0.46)		100.21	
Capv (6) (12)	46.44 (1.21)	0.67 (0.30)	50.44 (1.32)		97.55	
Maj (10) (5)	6.01 (0.53)	34.29 (0.70)	60.09 (0.59)		100.39	
Melt (30) (63)	37.49 (1.12)	18.88 (0.94)	5.01 (1.11)	38.62	100.00	60.17

(continued)

Table 3: Continued

Experiment	CaO	MgO	SiO ₂	CO ₂	Sum	Ca-no. ¹
<i>11 (CMS-CO₂-1); 26 GPa, 1850–1900°C, 30 min⁷</i>						
Mgpv (3) (27)	1.09 (0.32)	39.78 (0.42)	59.97 (1.05)		100.84	
Capv (3) (11)	43.54 (1.61)	3.41 (1.41)	47.54 (3.06)		94.48	
Periclase (3) (7)	0.05 (0.03)	99.93 (0.22)	0.06 (0.01)		100.04	
Mag (5)	2.54 (0.19)	39.89 (0.27)	0.04 (0.03)	57.57	100.00	4.35
Melt (25) (55)	21.49 (0.53)	28.50 (0.44)	11.24 (0.58)	38.76	100.00	35.12

AnhyB, anhydrous B; Cpx, clinopyroxene; En, enstatite; Maj, majorite; Mag, magnesite; Wad, wadsleyite; Rw, ringwoodite; Capv, calcium-silicate perovskite; Mgpv, magnesium-silicate perovskite; Periclase, MgO.

¹Ca-number is $\text{Ca}/(\text{Ca} + \text{Mg}) \times 100$ in molar units.

²The starting composition used is given in parentheses.

³Although melt was seen here, its interstitial nature prevented composition determination, and therefore modal proportions of phases are not provided.

⁴The number of analyses is given in parentheses.

⁵CO₂ in magnesite and melt calculated by difference.

⁶Second parentheses denote modal proportion.

⁷Magnesite here is from a lower temperature run performed at 1850°C. As shown in the text, the rest of this charge represents a mix of Mgpv-Capv-MgO, and hence phase compositions could not be reliably analyzed. The other phases, Mgpv, Capv, periclase, and melt, are from a higher temperature charge at 1900°C. Therefore, on this basis, the solidus is placed at 1875°C. Also, because only the composition of magnesite is determined at 1850°C, only the modal proportions of Mgpv, capv, periclase, and melt are provided.

However, on closer inspection, it can be distinguished from other phases by its dull grey appearance, subhedral outlines, and lack of fluorescence under the electron microprobe beam. Majorite is in contact with quench and is uniformly distributed throughout the charge. Periclase and magnesium perovskite are stable at 26 GPa. In backscatter images (Fig. 5), periclase occurs as a very dark phase, but can be distinguished from crystalline carbonate by its high relief and almost euhedral crystal outlines. Periclase rarely attains diameters of more than 10–15 µm. Magnesium-silicate perovskite (Fig. 5) is easily distinguished by its rather broken appearance, as reported in a previous experimental study by Walter *et al.* (2004), and it also exhibits damage under the electron beam. Magnesium-silicate perovskite ranges from 15 to 30 µm across. Both periclase and magnesium-silicate perovskite are found in contact with quenched liquid. In the system CMS–CO₂, at 16 GPa and 1475°C, an assemblage consisting of wadsleyite + cpx + anhydrous B + magnesite + melt (identified in Table 3) is seen, implying an isobarically invariant situation. At given contrast and brightness conditions, anhydrous B is much darker than wadsleyite, but can be easily distinguished from the other phases because of its much higher relief. In all the experimental charges, quenched melt not only occurs as segregated pools (Figs 1–5), but also as abundant interstitial melt pockets (Fig. 6). These melt pockets wet all the crystalline phase boundaries. Similar textures are also characteristic of experimental run products in the system CMAS–CO₂.

MELTING PHASE RELATIONS AND SEISMIC LOW-VELOCITY ZONES IN THE TRANSITION ZONE OF THE EARTH

In the experiments reported here in CMS–CO₂, the following phase assemblages defining the solidus are seen:

- 12 GPa : forsterite + clinoenstatite + cpx + magnesite + melt;
- 14 GPa : forsterite + majorite + cpx + magnesite + melt;
- 16 GPa : wadsleyite + majorite + cpx + magnesite + melt;
- 20 GPa : ringwoodite + majorite + Capv + magnesite + melt;
- 26 GPa : magnesium perovskite + periclase + Capv + magnesite + melt.

Although a definitive determinative analysis was not performed in this study, on the basis of previous studies in model systems (Presnall & Gasparik, 1990; Presnall & Walter, 1993; Canil, 1994; Presnall *et al.*, 1998), it is assumed that enstatite and majorite on the one hand, and forsterite and wadsleyite on the other, are in their respective *P–T* stability regions. Hence, even though we have only one experimental charge in the system CMS–CO₂ defining the solidus (in peridotite composition

Table 4: Experimental details, run products, and electron microprobe analyses (in wt %) of crystalline phases and quenched melts at the solidus of simplified carbonated peridotite in the system CMAS–CO₂

Experiment	CaO	MgO	Al ₂ O ₃	SiO ₂	CO ₂	Sum	Ca-no. ¹
<i>8 (CMAS–CO₂-21-A);² 10 GPa, 1475°C, 7 h</i>							
Forsterite (15) ³ (21)	0.23 (0.1)	56.69 (0.86)	0.04 (0.03)	42.49 (0.51)		99.45	
Cpx (11) (18) ⁴	15.03 (0.81)	26.79 (0.77)	0.41 (0.13)	57.61 (0.91)		99.84	
Gt (17) (9)	5.62 (0.79)	29.31 (1.01)	15.10 (0.84)	50.39 (0.61)		100.42	
Mag (14) (12)	5.21 (0.34)	40.06 (0.51)			54.73 ⁵	100.00	8.50
Melt (35) (40)	20.46 (1.34)	29.11 (1.21)	0.41 (0.1)	7.93 (1.67)	42.09	100.00	33.42
<i>9 (CMAS–CO₂-21-B); 10 GPa, 1525°C, 7.5 h</i>							
Forsterite (11) (23)	0.31 (0.13)	57.10 (0.73)	0.07 (0.05)	43.07 (0.65)		100.55	
Opx (13) (9)	3.11 (0.37)	37.46 (0.59)	0.39 (0.1)	58.81 (0.81)		99.77	
Cpx (9) (11)	14.79 (0.33)	27.01 (0.61)	0.52 (0.09)	57.10 (0.72)		99.42	
Gt (10) (12)	6.24 (0.66)	30.08 (0.49)	14.77 (0.60)	49.84 (0.49)		100.93	
Melt (40) (45)	18.98 (0.98)	30.51 (1.56)	0.45 (0.18)	8.17 (1.78)	41.89	100.00	30.76
<i>10 (CMAS–CO₂-23-A); 12 GPa, 1580°C, 7 h</i>							
Forsterite (9) (29)	0.19 (0.08)	57.14 (0.60)	0.03 (0.02)	41.99 (0.48)		99.52	
Opx (10) (11)	2.79 (0.56)	39.12 (0.67)	0.42 (0.13)	58.01 (0.71)		100.34	
Cpx (13) (12)	16.30 (0.59)	28.06 (0.83)	0.69 (0.21)	56.10 (0.69)		101.15	
Mag (9) (14)	6.21 (0.72)	41.13 (0.56)			52.66	100.00	9.73
Melt (30) (34)	23.12 (1.19)	28.93 (1.39)	0.32 (0.16)	5.29 (1.51)	42.34	100.00	36.33
<i>11 (CMAS–CO₂-23-B); 12 GPa, 1640°C, 5 h</i>							
Forsterite (13) (32)	0.28 (0.09)	57.22 (0.67)	0.03 (0.03)	41.99 (0.36)		99.52	
Opx (12) (13)	2.13 (0.50)	38.47 (0.39)	0.51 (0.18)	57.93 (0.66)		99.04	
Cpx (16) (8)	15.59 (0.42)	28.66 (0.58)	0.52 (0.19)	56.11 (0.70)		100.88	
Gt (13) (8)	7.12 (0.36)	31.10 (0.54)	13.12 (0.88)	48.69 (0.49)		100.03	
Melt (45) (39)	20.51 (1.60)	31.23 (1.89)	0.29 (0.19)	9.11 (2.04)	38.86	100.00	31.93
<i>12 (CMAS–CO₂-19-A); 14 GPa, 1625°C, 6 h</i>							
Forsterite (9) (16)	0.19 (0.07)	56.78 (0.31)	0.04 (0.03)	42.30 (0.44)		99.31	
Cpx (19) (30)	16.41 (0.37)	24.63 (0.51)	0.59 (0.18)	57.81 (0.44)		99.44	
Gt (13) (11)	5.09 (0.33)	28.76 (0.29)	13.82 (0.69)	51.94 (0.48)		99.61	
Mag (11) (12)	2.47 (0.52)	41.33 (0.83)	–	–	56.20	100.00	4.09
Melt (37) (31)	25.31 (1.17)	26.39 (1.49)	0.21 (0.17)	5.67 (1.73)	42.42	100.00	40.65
<i>1 (CMAS–CO₂-19); 14 GPa, 1675°C, 4 h</i>							
Forsterite (12) (10)	0.10 (0.03)	57.36 (0.26)	0.02 (0.02)	42.89 (0.39)		100.37	
Opx (9) (20)	2.16 (0.09)	38.39 (0.59)	0.26 (0.11)	59.50 (0.49)		100.61	
Cpx (15) (10)	14.96 (0.76)	27.24 (0.69)	0.36 (0.08)	57.41 (0.37)		99.97	
Gt (11) (10)	4.44 (0.29)	30.66 (0.44)	14.98 (0.37)	50.22 (0.51)		100.30	
Mag (10) (10)	3.12 (0.36)	39.45 (0.35)	–	–	57.43	100.00	5.34
Melt (30) (40)	23.77 (1.06)	28.39 (1.11)	0.32 (0.19)	8.84 (2.10)	38.68	100.00	37.42
<i>2 (CMAS–CO₂-14-A); 16 GPa, 1525°C, 5 h</i>							
Wad (13) (13)	0.29 (0.10)	56.99 (0.21)	0.10 (0.06)	43.01 (0.27)		100.39	
Cpx (12) (20)	20.99 (0.63)	23.50 (0.71)	0.50 (0.16)	55.02 (0.46)		100.01	
Gt (9) (20)	4.03 (0.21)	31.93 (0.50)	11.10 (0.13)	53.04 (0.79)		100.10	
Mag (10) (7)	4.51 (0.33)	43.48 (0.40)	–	–	52.01	100.00	6.88
Melt (30) (40)	38.10 (0.97)	16.98 (1.08)	0.50 (0.21)	4.10 (1.13)	40.32	100.00	61.48

(continued)

Table 4: Continued

Experiment	CaO	MgO	Al ₂ O ₃	SiO ₂	CO ₂	Sum	Ca-no. ¹
<i>3 (CMAS-CO₂-14-B); 16 GPa, 1575°C, 5 h</i>							
Wad (15) (13)	0.25 (0.03)	57.10 (0.21)	0.25 (0.11)	42.94 (0.31)		100.54	
Cpx (10) (15)	20.76 (0.84)	23.79 (0.78)	1.01 (0.51)	54.37 (0.69)		99.93	
Gt (10) (18)	5.80 (0.30)	31.56 (0.39)	12.01 (0.29)	51.95 (0.63)		101.32	
Mag (11) (6)	5.20 (0.41)	41.80 (0.39)	-	-	52.00	100.00	8.16
Melt (30) (48)	36.49 (0.81)	16.68 (0.91)	0.43 (0.29)	4.11 (1.04)	42.29	100.00	60.98
<i>4 (CMAS-CO₂-15-A); 20 GPa, 1650°C, 4 h</i>							
Rw (12) (16)	0.31 (0.09)	57.01 (0.35)	0.12 (0.10)	42.76 (0.42)		100.20	
Gt (10) (18)	4.10 (0.59)	34.30 (0.47)	7.50 (0.40)	54.70 (0.72)		99.00	
Capv (7) (22)	47.31 (0.79)	0.30 (0.21)	0.15 (0.11)	52.40 (1.13)		100.16	
Mag (10) (9)	3.10 (0.37)	43.98 (0.29)	-	-	52.92	100.00	4.79
Melt (33) (35)	39.23 (0.92)	17.56 (0.88)	0.31 (0.23)	3.65 (0.94)	39.25	100.00	61.47
<i>5 (CMAS-CO₂-15-B); 20 GPa, 1700°C, 2 h</i>							
Rw (10) (18)	0.40 (0.14)	57.11 (0.56)	0.09 (0.10)	43.07 (0.56)		99.87	
Gt (9) (19)	5.60 (0.44)	33.83 (0.51)	8.10 (0.60)	53.21 (0.55)		100.74	
Capv (9) (17)	46.11 (0.93)	0.37 (0.19)	0.11 (0.10)	52.51 (1.23)		99.10	
Mag (8) (5)	5.90 (0.41)	42.21 (0.37)	-	-	51.89	100.00	9.07
Melt (27) (41)	38.79 (1.02)	18.10 (0.76)	0.37 (0.30)	4.03 (0.89)	38.71	100.00	60.48
<i>6 (CMAS-CO₂-16-A); 26 GPa, 1850°C, 45 min</i>							
Mgpv (10) (20)	0.83 (0.29)	39.99 (0.49)	2.62 (0.23)	56.77 (0.76)		100.21	
Capv (6) (20)	46.59 (0.56)	1.34 (0.58)	2.56 (0.71)	48.19 (0.87)		98.68	
Periclase (4) (10)	0.17 (0.16)	98.88 (0.26)	0.40 (0.29)	0.02 (0.07)		99.47	
Mag (9) (10)	1.33 (0.34)	40.80 (0.61)	-	-	57.87	100.00	2.27
Melt (23) (40)	23.16 (1.12)	29.52 (0.88)	0.18 (0.12)	6.49 (0.71)	40.65	100.00	35.91
<i>7 (CMAS-CO₂-16-B); 26 GPa, 1900°C, 30 min</i>							
Mgpv (8) (18)	0.79 (0.31)	40.19 (0.33)	2.71 (0.30)	56.97 (0.81)		100.66	
Capv (8) (21)	45.67 (0.67)	3.97 (0.49)	2.27 (0.60)	47.23 (0.79)		99.14	
Periclase (5) (7)	0.09 (0.10)	98.45 (0.40)	0.31 (0.22)	0.02 (0.09)		98.87	
Mag (11) (11)	2.09 (0.23)	41.19 (0.70)	-	-	56.72	100.00	3.49
Melt (30) (43)	21.74 (1.02)	28.20 (0.69)	0.35 (0.20)	9.72 (1.20)	39.99	100.00	35.51

Opx, orthopyroxene; Cpx, clinopyroxene; Gt, garnet; Wad, wadsleyite; Rw, ringwoodite; Mag, magnesite; Capv, calcium-silicate perovskite; Mgpv, magnesium-silicate perovskite; Periclase, MgO.

¹Ca-number is $\text{Ca}/(\text{Ca} + \text{Mg}) \times 100$ in molar units.

²The starting composition used is given in parentheses.

³The number of analyses is given in parentheses.

⁴Second parentheses denote modal proportion.

⁵CO₂ in magnesite and melt calculated by difference.

space) wherein five phases were found (14 GPa and 1625°C; Table 3), and for the rest, the solidus was defined with two runs at low and high temperatures at each studied isobar, the melting phase relations in this system remain isobarically invariant. It should be noted that the above is true only for experimental runs defining the solidus of simplified carbonated peridotite (in this particular composition space). Other experimental runs that have phase(s) outside the composition space of interest (that is, simplified carbonated peridotite) are identified in Table 3.

Compared with CMS-CO₂, however, in the system CMAS-CO₂, different things happen (see below). As alumina (Al₂O₃) is added to the system CMS-CO₂ with the same phase assemblage present, the variance increases. In the system CMAS-CO₂, the melting relations of a peridotitic composition change from being isobarically invariant at 10–14 GPa (six phases) to isobarically univariant at 16–26 GPa (five phases). The reason for the change in variance is that there are six phases present along the solidus at 10–14 GPa, forsterite + orthopyroxene (opx) + clinopyroxene (cpx) + garnet + magnesite + melt. However,

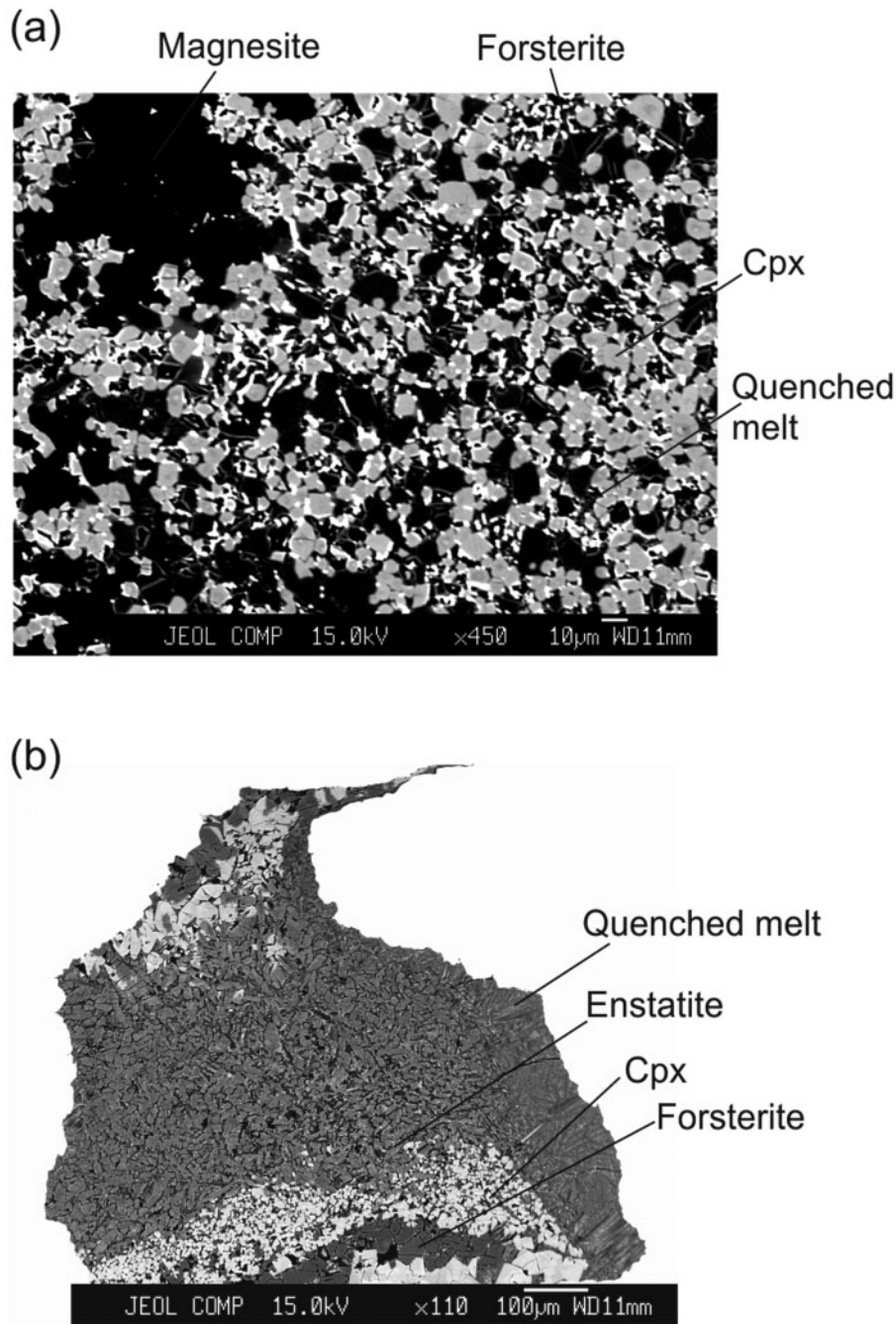


Fig. 1. Backscattered electron (BSE) images of experimental charges at 12 GPa and (a) 1550°C and (b) 1575°C. Quenched melt occurs as a coarse intergrowth of silicate and carbonate fractions. Magnesite is the darkest mass in the upper panel. Dark grey, medium grey, and light grey crystals are forsterite, enstatite, and clinopyroxene, respectively.

because opx disappears from peridotitic mantle above 14 GPa, there are only five phases (as listed below) that take part in defining the solidus reactions at 16–26 GPa. Hence, in P – T space, the solidus at 16–26 GPa occurs along a divariant surface, meaning that at these isobars a particular phase assemblage is stable over a certain temperature interval. The above also means that the solidus,

to some degree, depends on the bulk composition of the mantle analog in the system CMAS–CO₂. The main influence of adding Al₂O₃ to CMS–CO₂ is only to slightly dilute the liquid compositions reported here. In the system CMAS–CO₂, all the alumina is hosted in opx, cpx, garnet, calcium-silicate perovskite (capv or Capv), and magnesium-silicate perovskite (mgpv or Mgpv).

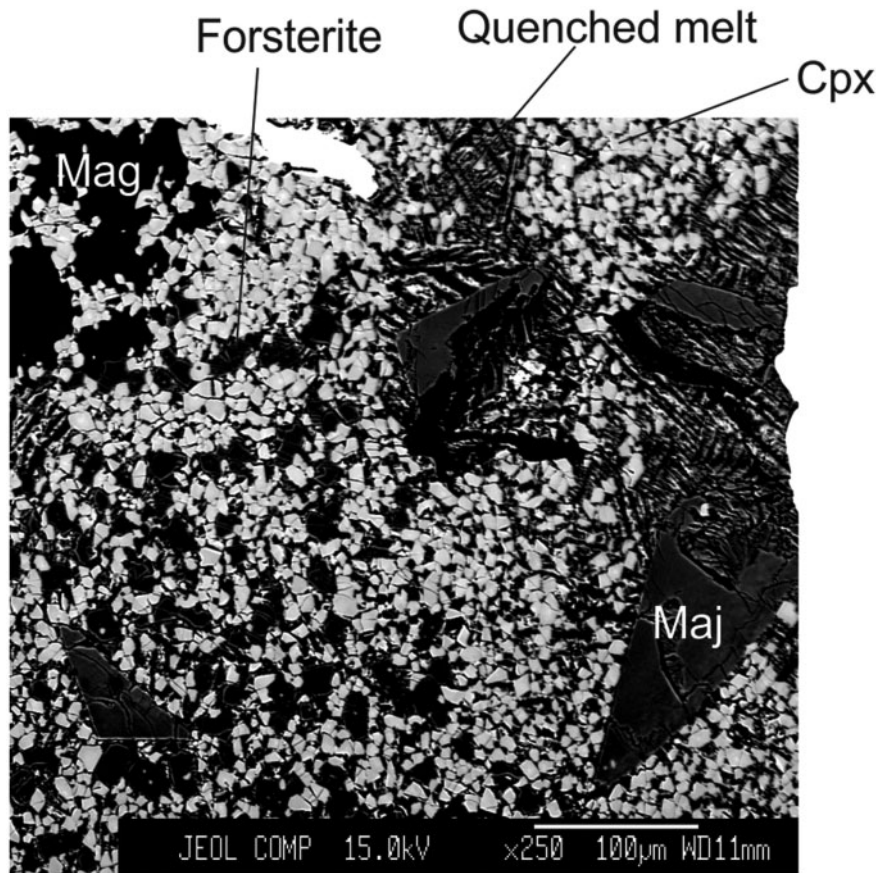


Fig. 2. BSE image of an experimental charge containing the solidus phase assemblage at 14 GPa and 1625°C, performed using a 14/8-type pressure cell. Quenched melt occurs as a coarse intergrowth of silicate and carbonate fractions. Melt generally occurs as segregated pools, but is also found interstitially. In this image, forsterite occurs as small (~10–25 µm), subhedral grains that are in general less dark than magnesite (Mag in the NW corner of the image). Majorite (Maj) occurs throughout the experimental run product as a medium grey phase, often subhedral and triangular in shape. Clinopyroxene (Cpx) is the lightest phase in this image.

Peridotitic mantle contains ~4% alumina, an amount that has only a small effect on the melting phase relations and liquid compositions. Hence, in theory, the solidus of a carbonated mantle peridotite composition with this amount of Al₂O₃ will only be slightly different from that in the system CMS–CO₂. With increasing pressure in the system CMAS–CO₂, we encounter the following solidus-defining assemblages:

- 10–14 GPa : forsterite + opx + cpx + garnet
+ magnesite + melt (isobarically invariant);
- 16 GPa : wadsleyite + cpx + garnet
+ magnesite + melt (isobarically univariant);
- 20 GPa : ringwoodite + garnet + Capv + magnesite
+ melt (isobarically univariant);
- 26 GPa : Mgpv + periclase + Capv
+ magnesite + melt (isobarically univariant).

As shown in Fig. 7, the most curious feature of the phase relations in the system CMS–CO₂ is an abrupt drop of

115–125°C in the solidus of model carbonated peridotite between 14 and 16 GPa. The solidus has a positive P – T slope between 12 and 14 GPa, above 16 GPa, and up to at least 26 GPa. Concomitant with the temperature drop between 14 and 16 GPa, the composition of the melt also changes significantly (Table 3; Fig. 8). At 12 and 14 GPa, the solidus melts are magnesiocarbonatites with Ca-number [molar Ca/(Ca + Mg) × 100] of about 40, whereas at 16 and 20 GPa, liquids at the solidus change to become highly calcic with Ca-number of roughly 61. This dramatic change in the melt composition, within an interval of 2–6 GPa, is puzzling as the coexisting crystalline carbonate continues to be nearly end-member magnesite with a limited amount of calcite solid solution (Table 3; Fig. 9). Hence, although magnesite contributes all the CO₂ to the melt, the melting reaction must include large amounts of a CaO-rich (lime) silicate as well because of the calcic composition of the melt. This behavior differs from that observed for the solidus of carbonate-bearing garnet peridotite in the system CaO–MgO–Al₂O₃–SiO₂–CO₂ (CMAS–CO₂) at lower pressures (3–8 GPa;

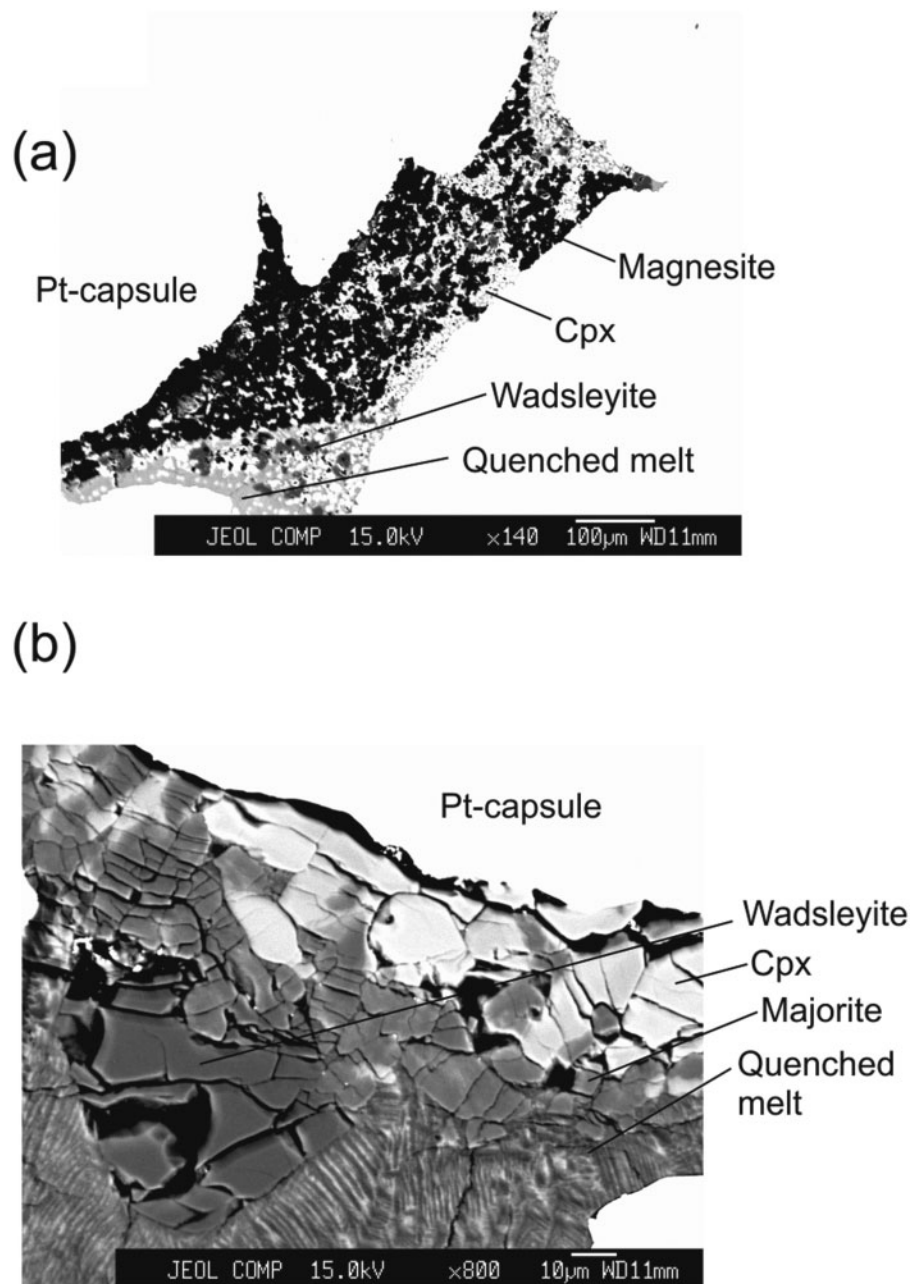


Fig. 3. BSE images of experimental charges at 16 GPa and (a) 1500°C and (b) 1525°C. Quenched melt occurs as a fine to medium intergrowth of silicate and carbonate fractions. In (a) magnesite is the darkest phase.

Dalton & Presnall, 1998; Gudfinnsson & Presnall, 2005), where contributions from magnesite (or other, compositionally different crystalline carbonate) are a larger part of the melting reaction. Also shown in Figs 7 and 8 and Table 3 are three other runs at 16 GPa in the system CMS–CO₂ and the experiment at 12 GPa and 1525°C. Here, the melt, in equilibrium with forsterite, cpx, and magnesite, is much too interstitial, and hence its composition could not be determined. Two more runs at 16 GPa,

1475°C and 1575°C, denoted as A and D, respectively in Fig. 7, warrant some attention here. The run at 1475°C contains an isobaric invariant assemblage consisting of wadsleyite + cpx + anhydrous B + magnesite + melt (Fig. 7; Table 3). The liquid, even though in equilibrium with wadsleyite and anhydrous B (two of the most magnesian crystalline silicates), is still highly calcic, with a Ca-number of about 63, and is hence only slightly more calcic than the runs at higher temperatures defining the

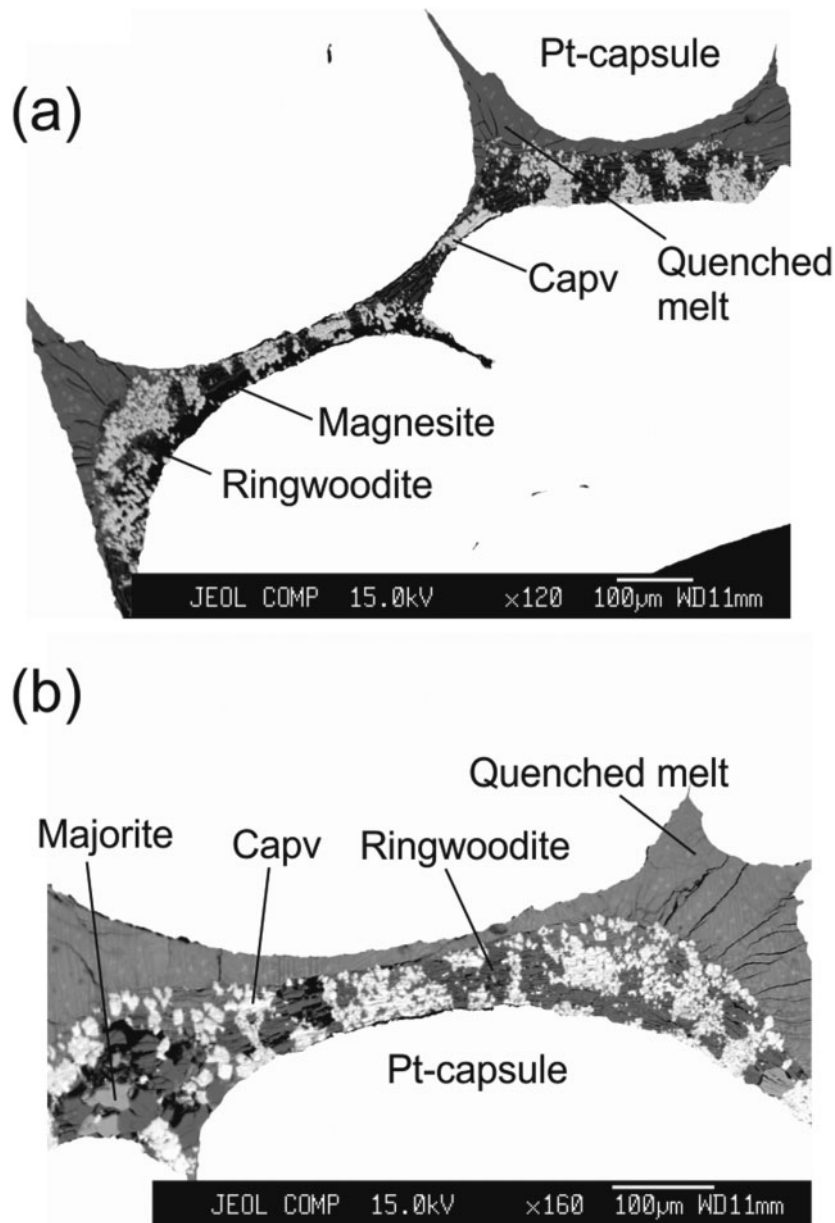
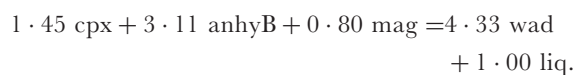


Fig. 4. BSE images of experimental charges at 20 GPa and (a) 1700°C and (b) 1750°C. Quenched melt occurs as a fine to medium intergrowth of silicate and carbonate fractions. Capv, calcium perovskite.

solidus (1510 and 1525°C, identified as B and C, respectively; Fig. 7) of simplified carbonated peridotite. Hence, as mentioned above, the melting reaction must include fairly large contributions from lime-bearing crystalline silicates. In fact, the reaction at this isobaric invariant point is



In this peritectic reaction, the coefficient of anhydrous B (anhyB) is greater than that of cpx and magnesite (mag),

only because the liquid (liq) is highly calcic, and hence an even greater amount of wadsleyite (wad) is produced upon melting.

Because anhydrous B is found as a stable crystalline phase in these experiments, a note on its stability in carbonated systems and from previous work on high-pressure melting of forsterite and enstatite is required. In experimental work related to mantle melting in a system consisting of MgO–SiO₂ (MS), we note that Presnall & Gasparik (1990; but see Kato & Kumazawa, 1986*a*, 1986*b*;

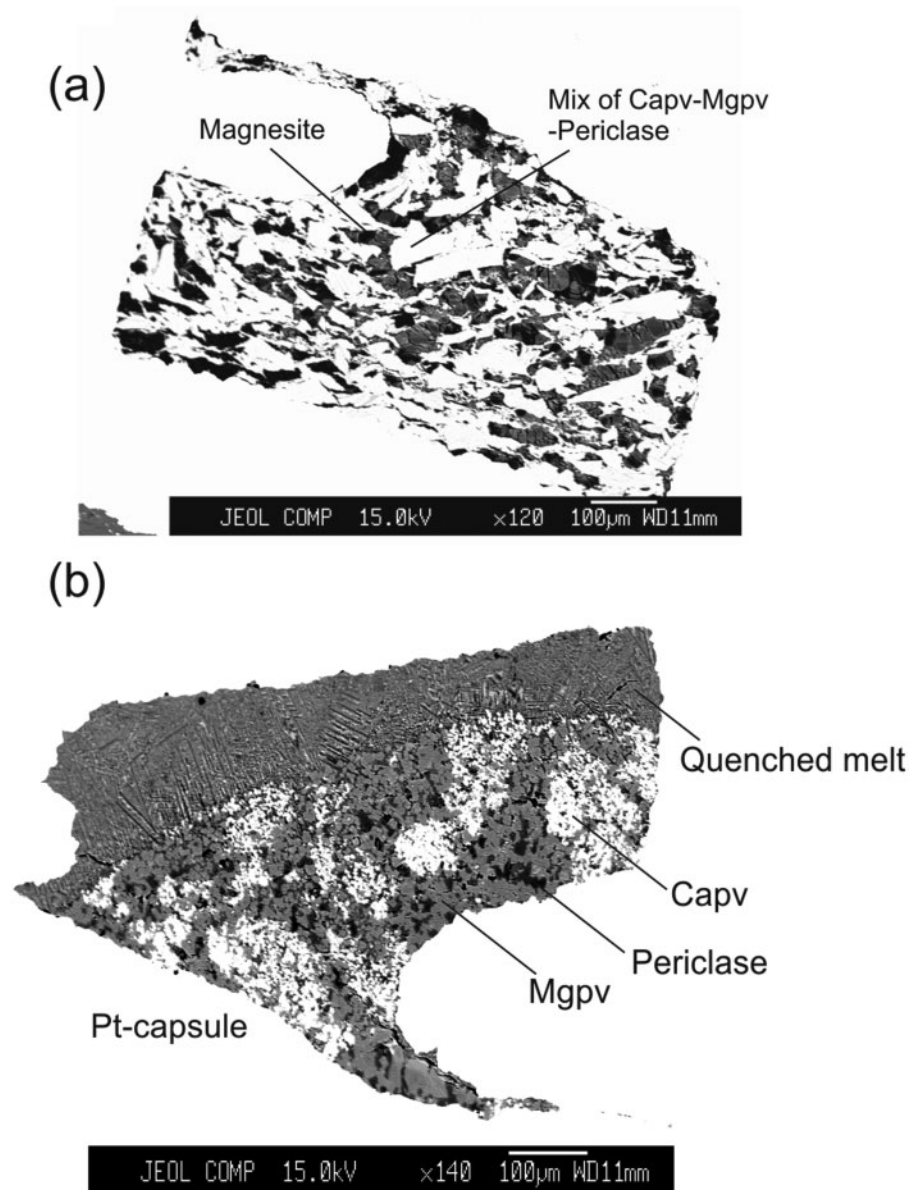


Fig. 5. BSE images of experimental charges at 26 GPa and (a) 1850°C and (b) 1900°C. Quenched melt occurs as a rather coarse intergrowth of silicate and carbonate fractions. Mgpv, magnesium perovskite.

Ito & Takahashi, 1987; Herzberg & Gasparik, 1989), and then Presnall & Walter (1993), in their high-pressure, high-temperature experimental work on clarifying the melting curve of end-member forsterite, enstatite, and their subsequent bearing on supposed early-Earth magma oceans and congruent or incongruent melting in the Earth, reported the presence of anhydrous B (along the melting curve) at pressures between 15.6 and 16.7 GPa. This pressure interval, in the above-mentioned studies, straddles the pressure datum at 16 GPa in the present study. The only difference between the systems volatile-free

(MS) and carbonated (CMS-CO₂) is that in the former, anhydrous B is found at much higher temperatures, 2310–2380°C; hence a difference of about 1000°C between the systems MS and CMS-CO₂ signifies the radical influence of carbon dioxide (this is also known from low-pressure studies) on the melting of dry mantle systems. The pressure cells used in the Presnall & Gasparik (Stony Brook, USA) and Presnall & Walter (Scarfe Laboratory, Edmonton, Canada) experiments are almost identical to the ones we used at Bayreuth, except that the previous experimental studies used rhenium (Re) capsules instead of

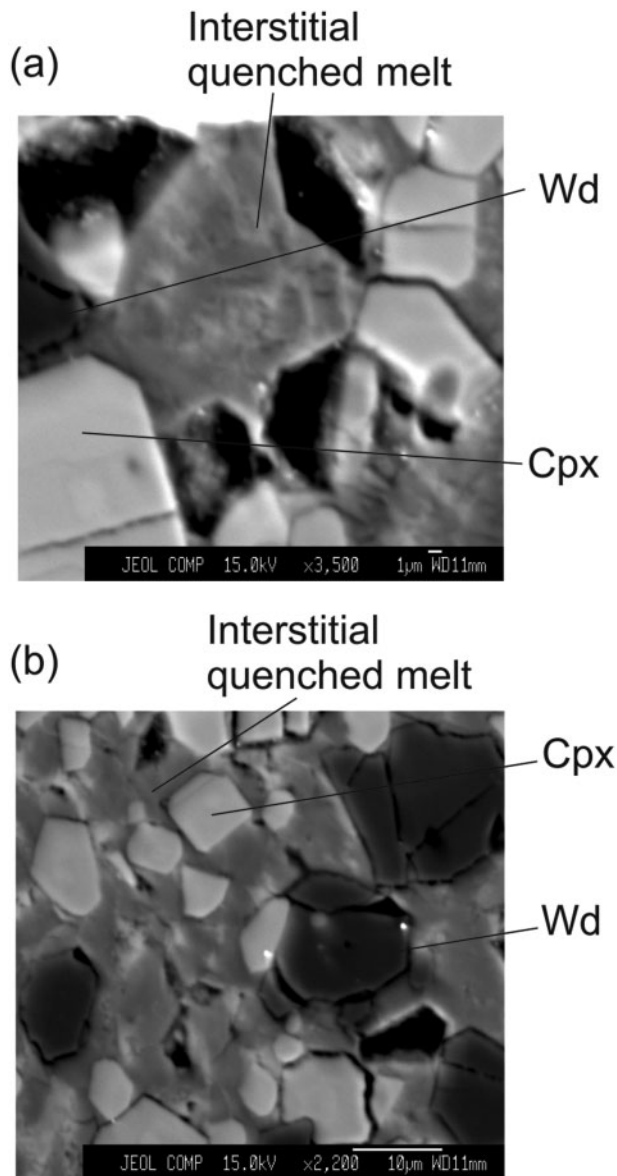


Fig. 6. (a, b) BSE images of experimental charges at 16 GPa. A fairly large amount of interstitial melt wets all the crystalline phase boundaries. Wd, wadsleyite.

platinum (this study), as rhenium has a much higher melting temperature than platinum, and is thus suited to act as a container when performing experiments at elevated P - T conditions in the refractory system MgO-SiO_2 . Therefore, on the basis of our work on CMS-CO_2 , an additional conclusion is that in liquid-bearing systems, lime and carbon dioxide when combined with MgO-SiO_2 do not appear to shift dramatically the pressure at which anhydrous B first becomes stable. This pressure overlap of incoming of a crystalline phase, in this case anhydrous B, in dry and carbonated systems in different experimental studies, performed in three laboratories, is encouraging.

At 16 GPa and 1575°C in the system CMS-CO_2 , liquid is in equilibrium only with wadsleyite and majorite. However, the liquid is still more calcic (Ca-number ~ 54 ; Fig. 8; Table 3), and is nowhere close to being as magnesian as that observed at lower (12–14 GPa) or higher (26 GPa) pressures. The calcic nature of the liquid compositions with increasing temperature determined over the 16 GPa isobar in the present study is similar to that observed in the work of Moore & Wood (1998), who presented melting phase relations of simplified carbonated peridotite in the system CMS-CO_2 at 3 GPa. In the experimental work of Moore & Wood, liquids, even though only in equilibrium with forsterite and opx, are fairly calcic. Also shown in Fig. 7 is the 7 GPa solidus invariant point (labelled 'A-P—unpub. work') of simplified carbonated peridotite in the system CMS-CO_2 of Arima & Presnall (unpublished work; mentioned by Dalton & Presnall, 1998). Considering that the pressure cells we used in our study are different from those used at University of Texas at Dallas (UTD), a straight lower pressure extension of our solidus will not pass through the Arima & Presnall datum. However, a close intersection is nearly achieved, and the joining of the Arima & Presnall datum with our experimental data would seem to indicate a slight to moderate curvature to the solidus, between 6 and 14 GPa, of simplified carbonated peridotite in the system CMS-CO_2 .

Initially, experimental runs in the system CMAS-CO_2 beginning only from 14 GPa were known. Therefore, once liquid and crystalline phase compositions in the system CMS-CO_2 became available, to constrain the topology of the solidus at pressures lower than 14 GPa, and thus also to furnish a more complete experimental dataset in the system CMAS-CO_2 , we have added four more experimental runs relevant for the solidus at 10 and 12 GPa shown in Fig. 10. To prepare starting mixtures (shown in Table 1) for determining the solidus at 10 and 12 GPa, in the system CMAS-CO_2 , the composition of phases obtained from CMS-CO_2 (this study), and those reported earlier on CMAS-CO_2 (Dalton & Presnall, 1998; Gudfinnsson & Presnall, 2005), were used. However, despite our best efforts to prepare starting mixtures that, when melted, would give six phases (including liquid that could be confidently analyzed by electron microprobe) in a particular capsule at 10–14 GPa, only at 14 GPa was isobaric invariance achieved. Therefore, at 10 and 12 GPa, four starting compositions had to be prepared (Table 1) that provided low and high temperature bounds on the solidus, suggesting that at such pressures a particular starting composition is perhaps less tolerant of the changes in P - T conditions. The same is also the case at 14 GPa, for which two runs are reported at 1625 and 1675°C. The run at 1625°C performed using CMAS-CO_2 -19-A (Table 1) that lacked opx in the experimental charge failed to give opx at 1675°C as well, so a new starting composition, CMAS-CO_2 -19, had

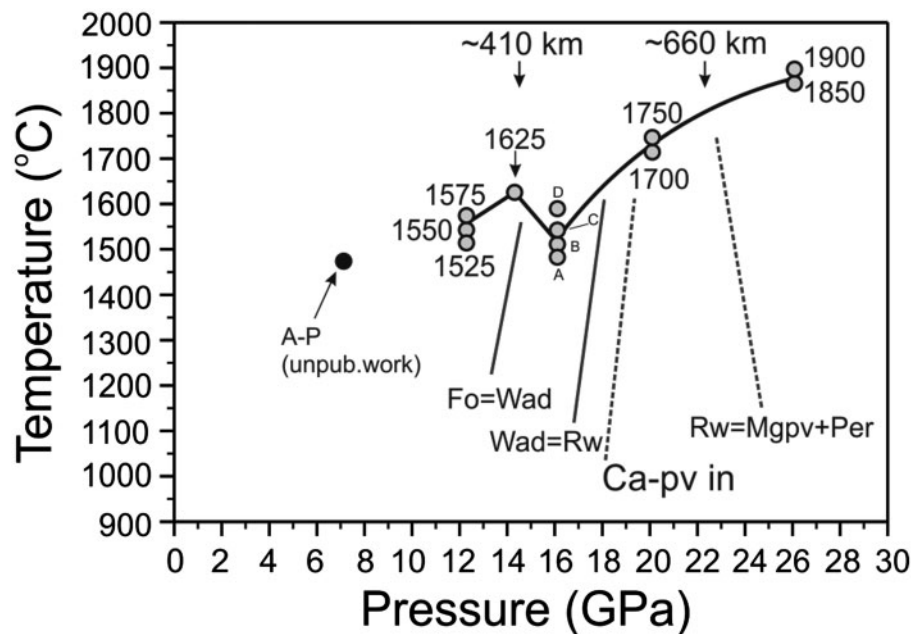


Fig. 7. The solidus of carbonated peridotite in the system CMS–CO₂ determined in this study (shown as a continuous line connecting filled grey circles). Numbers adjacent to the grey circles denote temperatures. The solidus at 12 GPa is constrained by three experimental runs (1525, 1550, and 1575°C), and is placed at 1550°C. Four experimental runs, denoted as A (1475°C, run 5 in Table 3), B (1510°C, run 6 in Table 3), C (1525°C, run 7 in Table 3), and D (1575°C, run 8 in Table 3), are shown at the 16 GPa isobar. At 1475°C (shown as A), anhydrous B is a stable crystalline phase coexisting with wadsleyite, cpx, magnesite, and melt. The solidus is bound between 1510°C (point B) and 1525°C (point C). At 1575°C (point D), liquid coexists with wadsleyite and majorite. Above 16 GPa, the solidus at 20 and 26 GPa is constrained by two experimental runs on the low- and high-temperature sides of the solidus curve at these isobars. The lower and upper experimental runs are 50°C apart at 20 and 26 GPa. At 26 GPa, magnesite (1850°C) was the only crystalline phase whose composition could be confidently determined. As described in the text, the rest of this charge represents a mix of Mgpv–Capv–MgO, and hence the compositions of each of these phases could not be analyzed. The other phases, Mgpv, Capv, periclase, and melt, are from a higher temperature charge at 1900°C. Therefore, on the basis of these two experimental runs, the solidus is placed at 1875°C. At 14 GPa, the run product contains the complete solidus assemblage, and is from 14/8-type pressure cell (shown with a downward pointing arrow next to 1625°C). For comparison, also shown is the 7 GPa and 1480°C solidus datum point of Arima & Presnall [unpublished work; shown here as a black filled circle labelled 'A-P (unpub. work)'; cited by Dalton & Presnall, 1998] in simplified carbonated peridotite (system CMS–CO₂). Projected in this figure are various boundary lines thought to be responsible for causing the seismically observed discontinuities at 410 km (forsterite–wadsleyite; downward pointing arrow), 520 km (wadsleyite–ringwoodite), and 660 km (ringwoodite to magnesium perovskite and periclase; downward pointing arrow; Presnall *et al.*, 1998; Fei & Bertka, 1999) in the Earth. Owing to disparate results regarding the slope of the boundary line at 660 km, it is shown as a dashed line (Fei & Bertka, 1999). The dotted line denoting 'Ca-pv in' projected onto this diagram shows the approximate *P*–*T* limit delineating the stability of calcium-silicate perovskite (Capv) in the Earth's mantle (peridotitic composition space), and has been adapted from an earlier study (Fei & Bertka, 1999). Fo, forsterite; Wad, wadsleyite; Rw, ringwoodite; Mgpv, magnesium perovskite; Per, periclase.

to be prepared that, upon melting, gave six phases. Similarly, in the pressure range of 16–26 GPa, every run reported required the preparation of a new starting composition. One would think that because opx disappears from the mantle carbonated peridotite analog studied here above 14 GPa, causing melting phase relations to become divariant, a particular starting composition would give the required phase assemblage over a temperature interval; however, as mentioned above and shown in Table 4, this is not the case. Notwithstanding these issues, as at 14 GPa, new experiments at 10 and 12 GPa were performed using the 14/8-type pressure cells at BGI. The results from the melting phase relations of carbonated peridotite in the system CMAS–CO₂ are presented in Table 4, and Figs 10 and 11. As is evident, very little change occurs when alumina is added to CMS–CO₂, in

so far as either the shape of the melting curve (Fig. 10) or the liquid compositions (Table 4; Fig. 11) are concerned. The shape of the carbonated peridotite solidus, as seen in CMS–CO₂, is maintained in CMAS–CO₂. Therefore, at 10–14 GPa, the melting curve has a positive Clapeyron slope, peaks at 14 GPa and 1675°C, and is then marked by a negative slope in the *P*–*T* projection (Fig. 10). Also shown in Fig. 10 is the 7 GPa solidus datum (identified with a slanting arrow pointing toward a filled black circle; denoted as D-P'98) of Dalton & Presnall (1998). In the pressure range of 16–26 GPa, the upper and lower filled grey circles in Fig. 10 represent the presence of magnesite at both of these temperatures; at these pressures, along an isobar, with increasing temperature beyond the upper grey circle, magnesite disappears, leaving liquid only with crystalline silicate–oxide phase assemblage.

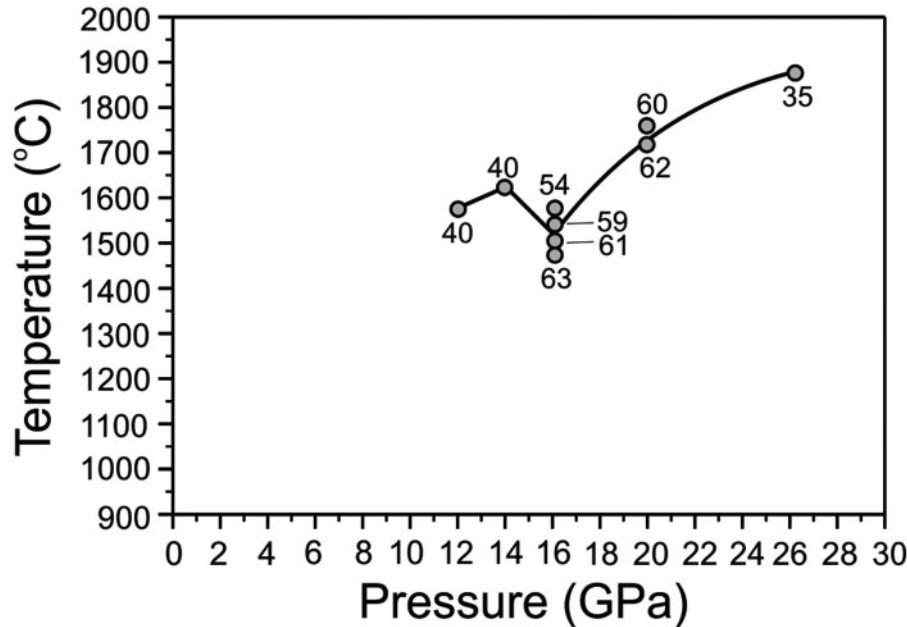


Fig. 8. Temperature–pressure plot (comparable with Fig. 7) showing the projected Ca-number [$\text{Ca}/(\text{Ca} + \text{Mg}) \times 100$ in molar units] of experimentally produced melts in equilibrium with various crystalline assemblages between 12 and 26 GPa, shown in Table 3. It should be noted that owing to the presence of interstitial melt (which could not be analyzed) in equilibrium with forsterite, cpx, and magnesite at 1525°C and 1550°C, the melt composition shown at 12 GPa is from that in equilibrium with forsterite, cpx, and enstatite at 1575°C, and hence, a minor interpolation is present in the solidus temperatures at 12 GPa. This is also the case for the 26 GPa solidus temperature and liquid composition. Of particular significance is the highly calcic nature of the melt (reflected in its Ca-number) at 16 and 20 GPa, in contrast to that formed at 12, 14, and 26 GPa. The experiment at 16 GPa and 1475°C contains wadsleyite + cpx + anhydrous B + magnesite + melt, and is slightly more calcic (63) than the two higher temperature runs (61 and 59) above it constraining the solidus. This experiment at 1475°C demonstrates that liquid in equilibrium with anhydrous B, a phase more magnesian than wadsleyite, is still calcic. The liquid coexisting with wadsleyite and majorite in the experiment at 16 GPa and 1575°C is less calcic (54) than the two runs below it, but still has a higher Ca-number than any liquid at 12, 14, or 26 GPa. It should be noted that owing to isobaric invariance at 14 GPa, only one liquid composition is shown.

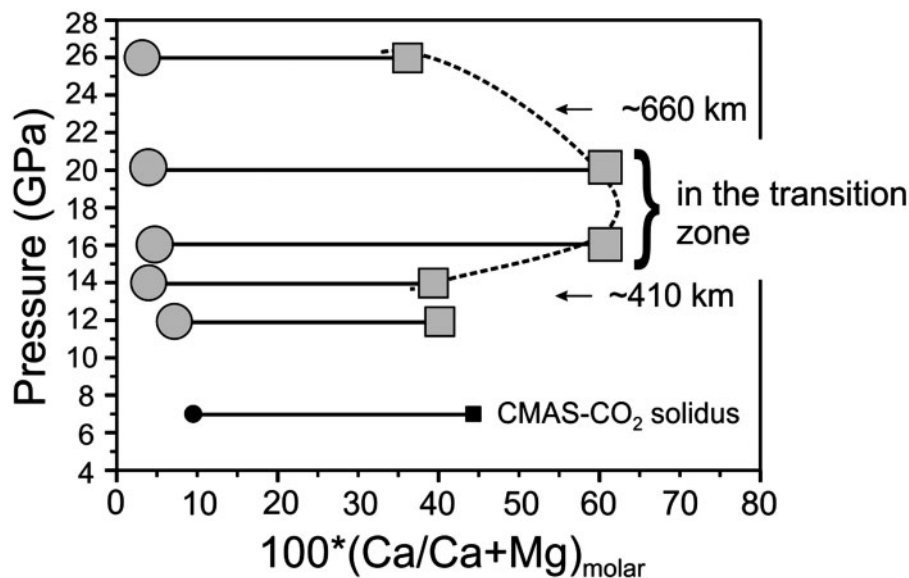


Fig. 9. Values of Ca-number for coexisting crystalline carbonate (grey circles) and melt (grey squares) as a function of pressure determined at the solidus of simplified carbonated peridotite in the system CMS–CO₂ (this study). To facilitate visualization, liquid compositions are shown simply where either isobaric invariance was achieved (for instance, 14 GPa) or as an average of two liquids (16 and 20 GPa), where the solidus was constrained by runs at the low- and high-temperature sides at a particular isobar. At 12 and 26 GPa, liquid compositions have been interpolated. Also shown for comparison are the crystalline carbonate (filled black circle) and liquid (filled black square) compositions determined at the solidus of simplified carbonated peridotite in the system CMAS–CO₂ at 7 GPa (Dalton & Presnall, 1998). The dashed curve shows the changes in melt composition with increasing pressure, and is only to aid visualization. It should be noted that the 14 GPa data shown in this panel are from an experimental run performed in 14/8-type pressure cells.

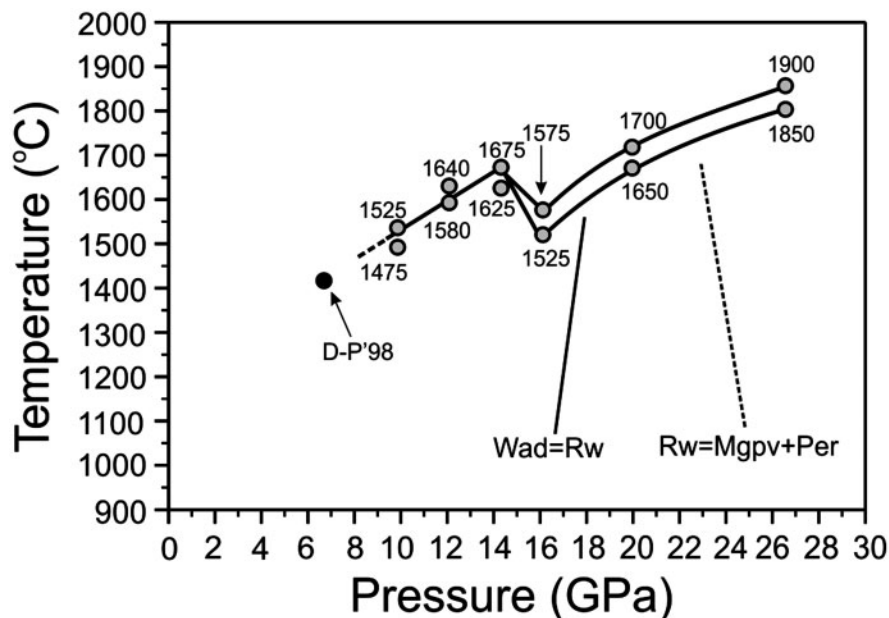


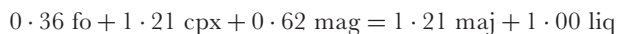
Fig. 10. The solidus curve for simplified carbonated peridotite in the system CMAS–CO₂ as determined in this study. At 10 and 12 GPa, the melting curve is constrained by runs from lower and higher temperature experiments. At 14 GPa, two experimental runs are shown, 1625 and 1675°C (Table 4). At 1625°C, the charge consists of forsterite + cpx + garnet + magnesite + melt. However, at 1675°C, isobaric invariance was achieved (Table 4). Experiments at 10–14 GPa were performed using 14/8-type pressure cells. As a result of the disappearance of opx from peridotitic mantle, melting phase relations become divariant in this part of the composition space, and hence, span a surface (shown with two filled grey circles at 16, 20, and 26 GPa). Therefore, owing to this change in variance, there are two continuous lines originating from the 14 GPa invariant point, signifying the beginning of the divariant surface over which carbonated mantle peridotite exists. The divariant surface continues to exist at least up to 26 GPa. Numbers next to the grey circles denote temperature. At 16 GPa, the high-temperature run (1575°C) is shown with a downward pointing arrow. The lower pressure extension of the solidus curve in CMAS–CO₂ (this study) is shown as a dashed line originating from 10 GPa. A solidus datum from Dalton & Presnall (1998) for simplified carbonated peridotite in the system CMAS–CO₂ is shown at 7 GPa and 1430°C (filled dark circle; D-P'98). For clarity, only boundary lines denoting the wadsleyite–ringwoodite phase transformation (~520 km in the Earth) and dissociation of ringwoodite to a mixture of Mgpv plus periclase (~660 km in the Earth) are shown in this figure (adopted from Fei & Bertka, 1999).

Once magnesite disappears with increasing temperature, the solidus is no longer constrained in the P – T plane, and hence by extension, the definition of the solidus is no longer valid. A further consequence of magnesite disappearing is that the liquid compositions are also no longer tied in the P – T plane, similar to what happens in the system CMS–CO₂ at 16 GPa and 1575°C. As shown in Fig. 11, liquid compositions in the system CMAS–CO₂ are almost identical to those seen in the system CMS–CO₂, except that liquids in the system CMAS–CO₂ are slightly aluminous. Phase compositions in the system CMAS–CO₂ in the pressure range 10–26 GPa are reported in Table 4.

Using the composition data provided here, the calculated melting reactions of carbonated peridotite in the system CMS–CO₂ at different pressures are as follows:



14 GPa:



16 GPa:



20 GPa:



26 GPa:



In these reactions, the following abbreviations are used: fo, forsterite; maj, majorite; rw, ringwoodite; capv, calcium-silicate perovskite; per, periclase; mgpv, magnesium-silicate perovskite. It can be seen that the solidus melting reactions at all pressures are of the peritectic type, as at 16 GPa and 1475°C (the anhydrous B-bearing run). In the reactions listed above, as magnesite provides all the CO₂ for the melt to make it carbonatitic and the concentration of CO₂ in the melt does not change much, the amount of magnesite in the melting reactions is nearly constant. Whereas clinoenstatite (En = CEn; CEn = clinoenstatite) and majorite are produced upon melting at 12–20 GPa, magnesium perovskite is in reaction

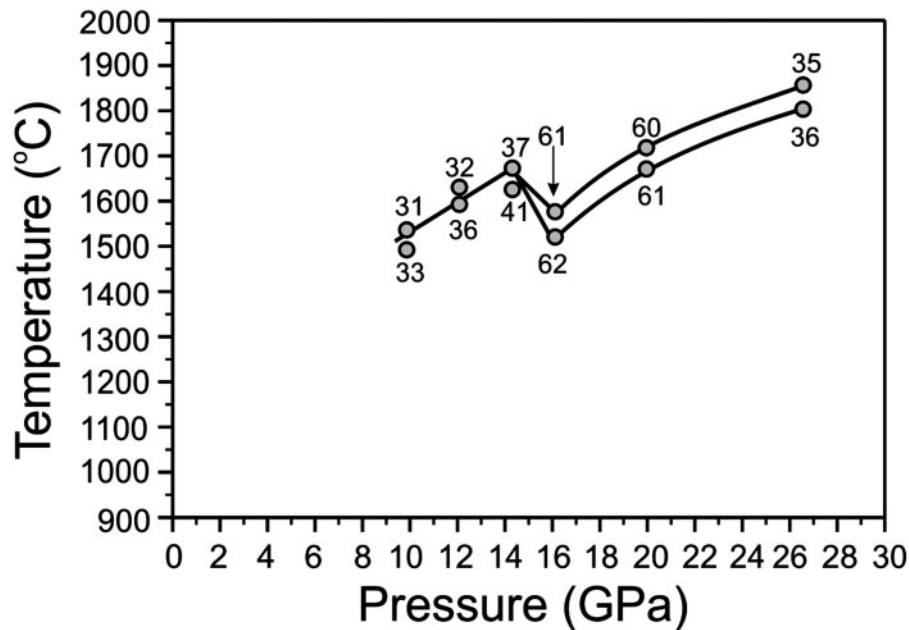


Fig. 11. Temperature–pressure projection showing the composition of liquids in terms of their Ca-number for melting of simplified carbonated peridotite in the system CMAS–CO₂ as determined in this study. Numbers next to grey circles represent the Ca-number of a particular liquid. A downward-pointing arrow (16 GPa) denotes the liquid composition from a run at 1575°C. Addition of alumina to CMS–CO₂ does not cause radical changes in the liquid compositions in the two studied systems, CMS–CO₂ (shown earlier) and CMAS–CO₂.

with the melt at 26 GPa. An interesting feature of the melting reactions at 16 and 20 GPa is the relatively large contribution of silicate phases to liquid production, a feature also evident when we are outside the mantle peridotite analog, for example when anhydrous B is a stable crystalline phase at 16 GPa and 1475°C. These reactions are different from those determined in lower pressure work, either in simplified carbonated peridotite (Dalton & Presnall, 1998; Wyllie & Lee, 1998; Gudfinnsson & Presnall, 2005) or model eclogite [a review has been given by Luth (2006)] in which crystalline carbonate overwhelmingly exerts its influence on the solidus and liquid compositions. In the present study, by 26 GPa, magnesite has a slightly greater contribution to melt production.

The modal proportions of phases in our experiments are shown in Tables 3 and 4. As a cautionary note, the composition of phases in the system CMS–CO₂ (Table 3) needs some clarification. At 12 GPa and 1525°C or 1550°C, the interstitial nature of the melt prevented the reliable determination of its composition, and hence the modal proportions of the other phases could not be calculated. Also, at 26 GPa and 1850°C, the charge consisted of dark magnesite and an intricate mixture of magnesium perovskite, calcium perovskite, and periclase. We are not certain if this is a liquid-present run. However, at 1900°C, abundant melt plus magnesite perovskite, calcium perovskite, and periclase are present. Therefore, on the basis of these two runs, the solidus is placed at 1875°C. Also, the modal

proportions shown in Table 3 (for CMS–CO₂) are only for phases present at 1900°C. Because at 1850°C only the composition of magnesite is known, the melting reaction shown above has some uncertainty. Therefore, since the liquid compositions at 12 GPa and 1525–1550°C, and 26 GPa and 1850°C are not known, there is some interpolation involved in all the projection diagrams.

In both the systems CMS–CO₂ and CMAS–CO₂, melts at 16 and 20 GPa are more calcic (Figs 8, 9 and 11; Tables 3 and 4) than those along the solidus of model carbonated peridotite in the system CMAS–CO₂ at lower pressures (3–8 GPa; Dalton & Presnall, 1998; Gudfinnsson & Presnall, 2005), alkalic-multicomponent peridotite (Ghosh *et al.*, 2009), and carbonated peridotite in CMASN–CO₂ (Litasov & Ohtani, 2009). This difference in the liquid composition reported here and by Ghosh *et al.* (2009) and Litasov & Ohtani (2009), cannot simply be an artefact of the starting mixture employed, or different concentrations of Fe (iron), Na (sodium), and K (potassium), three elements that are likely to affect the solidus temperatures to some extent, in the above-mentioned two studies, as long as the relevant phase assemblage is maintained. Although adding Fe, Na, and K to the starting compositions will dilute the liquid compositions to a certain degree, it is unlikely that either the shape of the solidus or the melt composition we report here will radically differ (especially at 16 and 20 GPa) from the data of Ghosh *et al.* (2009) on the one hand, and

those of Litasov & Ohtani (2009) on the other. This is especially so as we have noted liquid compositions changing, not only in CMS–CO₂ (at 16 GPa, with increasing temperature), but additionally in the system CMAS–CO₂ (Fig. 11). For example, as reported earlier, the low-pressure ‘carbonated peridotite solidus ledge’ in the system CMS–CO₂ [reviews have been given by Wyllie & Lee (1998) and Luth (2006)], does not disappear with adding more chemical complexity (Falloon & Green, 1989).

Melt compositions at 16 and 20 GPa are almost identical to those of calcio-carbonatites (molar Ca-number starting from 60) seen on the Earth’s surface. This resemblance is purely coincidental, and should not be viewed as a suggestion that calcio-dolomitic carbonatites on the Earth’s surface are derived from such depths in the Earth. The resemblance implies that the choice of studied systems here is relevant to lavas we are most familiar with. In both the studied systems, decreasing Ca-number of the liquid compositions at 10, 12, 14, and 26 GPa is documented in this study, results that are fairly consistent with low-pressure work, either on CMAS–CO₂ (Dalton & Presnall, 1998) or the end-member CaCO₃–MgCO₃ join (Buob *et al.*, 2006). However, between 14 and 16 GPa, there appear to be radical changes in the phase relations, seen as sharp breaks, both in the liquid compositions and melting reactions. At present, it is not clear what changes are occurring in the phase stability between 14 and 16 GPa to cause the solidus to decrease abruptly and produce calcic liquids.

To ascertain that the abrupt drop in the solidus temperature as noted above is not a function of changing cell-type across 14–16 GPa (14/8 to 10/5), we performed additional confirmation experiments. Experiments at 14 GPa in the system CMS–CO₂ were performed using two types of pressure cell. Experiments that used 14/8 cells produced the isobarically invariant solidus assemblage consisting of forsterite + clinopyroxene + majorite + magnesite + melt, as described above (Fig. 2). With the 14/8-type pressure cell, this solidus phase assemblage occurs at 1625°C. Using 10/5 pressure cells, we can provide only lower and upper bounds on the solidus temperatures. For example, at 1625°C, the run products consist of forsterite, cpx, magnesite, and interstitial quenched melt (Fig. 12, upper panel). Owing to their small amount and interstitial nature, we do not have electron microprobe analyses of these melt pockets. At 1650°C, the experimental run consists of forsterite, cpx, majorite, and quenched melt (Fig. 12, lower panel). This higher-temperature run lacks magnesite. On the basis of these two runs, we have placed the solidus at 1635°C. Therefore, the solidus temperature, using 10/5 pressure cells, is within temperature uncertainty of the determinations using 14/8-type pressure cells. The experimental observation that solidus temperatures, using two types of pressure cells, practically overlap each other indicates that

the original solidus temperature using a 14/8-type pressure cell (as described above) is a correct determination. The solidus determinations using two types of pressure cells also provide a sense of the temperature precision in the experiments reported here. The compositions of phases in these two runs performed using 10/5 pressure cells are provided in Table 5.

Another noteworthy feature of the phase relations is that, whereas liquids show abrupt excursions in their composition, the coexisting crystalline carbonate in equilibrium with these carbonatitic melts remains magnesite with molar Ca-number of roughly 2–10 (Tables 3 and 4; Fig. 9). At lower pressures the crystalline carbonate in equilibrium with the carbonatitic liquid seemingly shows a regular change in its composition comparable with that of the melt composition, becoming more magnesian with increasing pressure (see Dalton & Presnall, 1998, fig. 6). However, once the dolomite–magnesite transition at the solidus of carbonated peridotite in CMAS–CO₂ has gone to completion, the crystalline carbonate, in the pressure range of 5–7 GPa, does not vary radically in its composition. It is the liquid that continues to become more magnesian from 5 to 7 GPa (see Dalton & Presnall, 1998, fig. 6), a feature in simplified carbonated peridotite that appears to reflect what is happening on the CaCO₃–MgCO₃ join at similar pressures (Buob *et al.*, 2006). However, although it might be of great use to directly compare liquid compositions on the carbonate–silicate joins with those on the CaCO₃–MgCO₃ join, as Luth (2006) pointed out, such a comparison has some problems.

Taken together, a reinforcing conclusion is that, although the presence of crystalline carbonate has a large influence on the melting temperature of carbonated peridotite and gives the melts their carbonatitic character, the variation in the Ca-number of the melts in the studied pressure range appears to be primarily caused either by changes in the stability of the silicates or by fairly dramatic changes in the carbonate phase diagram at these elevated pressures. Therefore, in our opinion, one of the pressing needs is to extend the carbonate (end-member) phase diagram to more elevated pressures; some holes in this respect are starting to become filled-in (e.g. Buob *et al.*, 2006). To understand what might be causing the shape of the solidus curve in the present study an approach that might work would be to section the systems CMS–CO₂ and CMAS–CO₂ even further, and investigate various segments separately, as has been done recently to resolve the solidus positions of carbonated mafic rocks (Luth, 2006, 2009). Grassi & Schmidt (2011) observed a temperature depression along the solidus (approximately between 13 and 16 GPa) of multicomponent pelite, and the disappearance of cpx, formation of sodium-rich crystalline carbonate, and change of melting from fluid-absent to fluid-saturated; these were three main reasons proposed to explain the

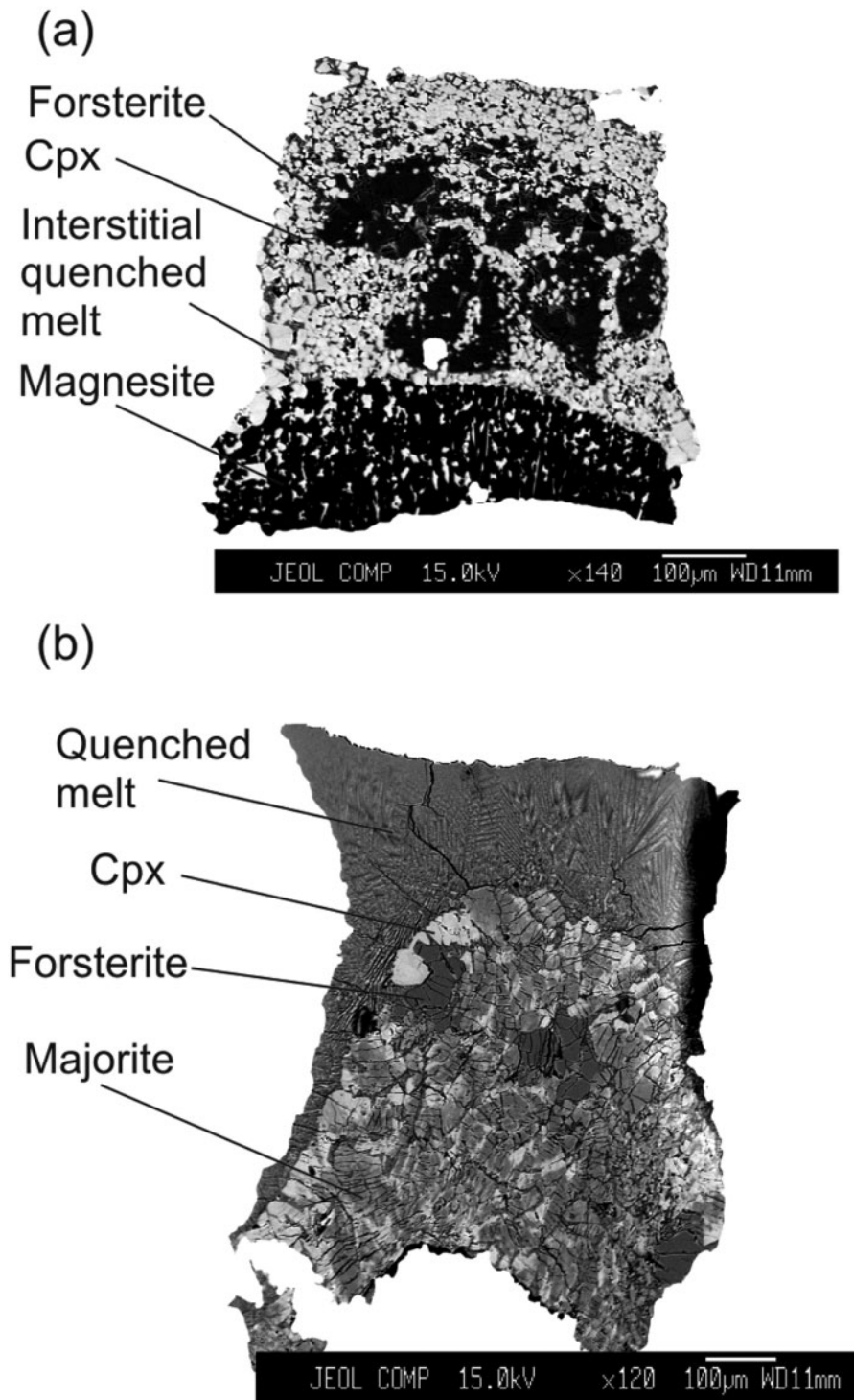


Fig. 12. BSE images of experimental runs at 14 GPa and (a) 1625°C and (b) 1650°C. These runs were performed in 10/5-type pressure cell, and therefore are confirmations of those performed using 14/8-type pressure cells (described in the text). These runs demonstrate that the solidus determined using two types of pressure cell is within temperature uncertainty.

Table 5: Experimental details, run products, and electron microprobe analyses (in wt %) of crystalline phases and quenched melts at the solidus

Experiment	CaO	MgO	SiO ₂	CO ₂	Sum	Ca-no. ¹
<i>1 (CMS-CO₂-7);² 14 GPa, 1625° C, 5 h</i>						
Forsterite	0.13	56.83	42.39		99.34	
Cpx	20.07	22.70	56.49		99.53	
Mag	4.22	38.26	0.21	57.31 ³	100.00	7.30
<i>2 (CMS-CO₂-7); 14 GPa, 1650° C, 5 h</i>						
Forsterite (14) ⁴	0.13 (0.02)	57.05 (0.18)	42.77 (0.17)		99.95 (0.29)	
Cpx (14)	12.87 (0.53)	29.13 (0.46)	57.80 (0.16)		99.81 (0.26)	
Maj/En (16)	1.99 (0.63)	38.28 (0.58)	59.76 (0.19)		100.02 (0.33)	
Melt (50)	21.02 (1.13)	26.76 (1.62)	17.29 (1.45)	34.93	100.00	35.94

These experiments were repeated using 10/5 pressure cells, and suggest that the solidus temperatures of carbonated peridotite determined using either 14/8 or 10/5 pressure cells are within temperature uncertainty. Cpx, clinopyroxene; En, enstatite; Maj, majorite; Mag, magnesite.

¹Ca-number is Ca/(Ca + Mg) × 100 in molar units. Results shown are bracketed experimental runs.

²The starting composition used is given in parentheses.

³CO₂ in magnesite and melt calculated by difference.

⁴Number of analyses is given in parentheses.

shape of this melting curve. However, in our work, cpx continues to be a stable, equilibrium crystalline phase, and disappears from the mantle solidus somewhere between 16 and 20 GPa, a pressure interval in which the cpx to calcium-silicate perovskite transition perhaps occurs (see Fei & Bertka, 1999). Hence, as the system studied here lacks fluid (unlike the Grassi & Schmidt study), and also because the solidus has a positive slope between 16 and 20 GPa, the disappearance of cpx is perhaps not causing the cusp in the solidus between 14 and 16 GPa observed here. If indeed the observed solidus cusp is explicable in terms of the disappearance of cpx and the appearance of calcium-silicate perovskite, then such a feature would develop in the pressure interval 16–20 GPa, not below it. In addition, the predicted disappearance of cpx still does not explain the calcic nature of the experimental liquids observed at 16 and 20 GPa. However, despite the above, it is still possible that the disappearance of cpx from the solidus assemblage is responsible for the cusp observed in this study.

Shown in Fig. 7 are univariant boundary lines delineating the iso-chemical phase transformations for forsterite–wadsleyite, wadsleyite–ringwoodite, and the dissociation of ringwoodite to magnesium perovskite and periclase that are thought to be responsible for causing seismic discontinuities at approximate depths of 410, 520, and 660 km in the Earth (Fei & Bertka, 1999). A comprehensive phase diagram over a fairly large P – T range, in the system MgO–SiO₂ wherein the above-mentioned phases appear has been given by Presnall *et al.* (1998). It should be noted that the three boundary lines are drawn in the

system MgO–SiO₂, and therefore their intersection with the solidus curve, either in CMS–CO₂ (Fig. 7) or in CMAS–CO₂ (Fig. 10), is approximate. When such boundary lines intersect other curves, creation of cusps in P – T space is theoretically required. At present we do not have sufficient phase equilibrium data for precise determination of the form of these cusps at the solidus, and hence the boundary lines are not extended to the two solidi determined in the present study. Additionally, in Fig. 13, we compare the solidus of simplified carbonated peridotite in the system CMS–CO₂ determined here with two recent solidus determinations at comparable pressure conditions (Litasov & Ohtani, 2009; Rohrbach & Schmidt, 2011). Whereas Litasov & Ohtani (2009) reported solidus determinations in the system CMAS–Na₂O–CO₂ (CMASN–CO₂) at 10.5, 16.5, 20, 27, and 32 GPa, Rohrbach & Schmidt (2011), in a multicomponent system, determined the solidus of carbonated peridotite at 10, 14, and 23 GPa. An essential feature of these two experimental studies is the apparently flat nature of the reported solidus of carbonated peridotite.

Changes in the carbonated peridotite solidus between 12 and 26 GPa have fundamental consequences for the petrology, geochemistry, and seismology of the mantle at these and greater pressures. For example, if interconnection of carbonatitic melts occurs as readily at Transition Zone and lower mantle pressures as it seemingly does at upper mantle pressures (Minarik & Watson, 1995), carbonatite magmas are likely to segregate from their source at very low melt fractions. Measured partition coefficients of light rare earth elements (LREE) and large ion

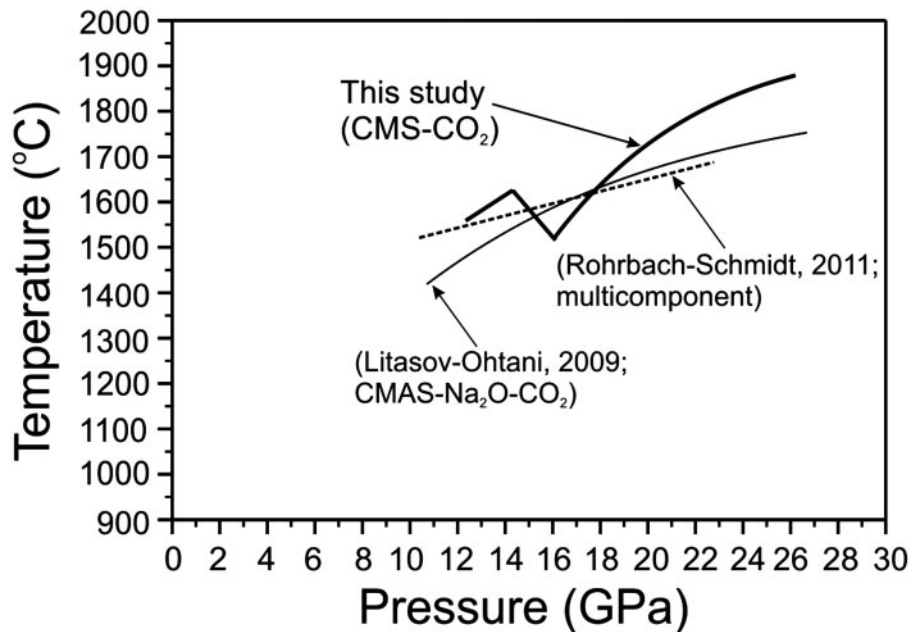


Fig. 13. Temperature–pressure projection showing the solidi of carbonated peridotite in three studies: the present work, shown as ‘This study (CMS–CO₂)’; Litasov & Ohtani (2009) in the system CMAS–Na₂O–CO₂; Rohrbach & Schmidt (2011) in a multicomponent system. Litasov & Ohtani (2009) reported their solidus determination at 10.5, 16.5, 20, 27, and 32 GPa, and Rohrbach & Schmidt (2011) reported their solidus determination at 10, 14, and 23 GPa.

lithophile elements (LILE) between Transition Zone minerals (cpx and majoritic garnet) and carbonated magmas suggest that all the LREE and LILE are highly incompatible in these solid phases (Keshav *et al.*, 2006, unpublished data; Walter *et al.*, 2008), and extraction of these magmas would leave a highly trace-element depleted residue. Although the precise mechanism is unknown, such melts would invariably metasomatize the surrounding mantle, resulting in the development of a variety of geochemical reservoirs over time, in particular the source regions of other silica-undersaturated magma types, including kimberlites and ocean-island basalts. Modeling results suggest that kimberlites tap a mantle source that has been enriched in trace elements from melts resembling carbonatites (Keshav *et al.*, 2005). Therefore, if kimberlites are derived from the Transition Zone and the lower mantle, trace element pre-conditioning in the source is a prerequisite. Small-degree mantle melting would also affect the relationship between major and trace elements in larger-degree mantle melts, as has been postulated for the shallower mantle (McKenzie, 1984; Presnall *et al.*, 2002; Presnall & Gudfinsson, 2005). By virtue of being small-degree melts, extraction of these magmas would have very little effect on the major-element composition of the mantle from which they were derived.

Melting caused by the negative slope of the carbonated peridotite solidus will also influence seismic velocities in the Transition Zone of the Earth. In Fig. 14, we show two assumed solid adiabats for ‘normal’ mantle with a potential

temperature (T_p) of 1350 and 1400°C and a gradient of 13°C GPa⁻¹ (Katsura *et al.*, 2004). Intersection of these adiabats with the carbonated peridotite solidus would cause melting at ~600 and 550 km, respectively. When these adiabats are just above the solidus, the amount of melting will be very small. At slightly shallower depths, where the adiabats lie at increasingly higher temperatures above the solidus, enhanced melting will take place. We do not have sufficient data above the solidus for precise modeling of the degree of melt that might result, but it could be of the order of ~0.5–1%. In Fig. 14 we show the depth ranges of seismic low-velocity zones deep in the mantle from various locations. There are dominantly two depth ranges for deep low-velocity zones shown in Fig. 14. Some are restricted to a depth range of ~350–600 km (Nolet & Zielhuis, 1994; Vinnik *et al.*, 1996, 2004, 2005; Sieminski *et al.*, 2003; Vinnik & Farra, 2006), corresponding almost exactly to the depth range in which the solidus of carbonated peridotite abruptly decreases. We propose that these low-velocity anomalies are due to melting associated with the depression of the solidus of carbonated peridotite. However, there are other low-velocity regions that have been detected at an approximate depth of ~350–370 km (Revenaugh & Sipkin, 1994; Vinnik & Farra, 2002, 2007; Song *et al.*, 2004; Courtier & Revenaugh, 2007). These require a different explanation, as they occur consistently at a pressure range below that of the solidus dip.

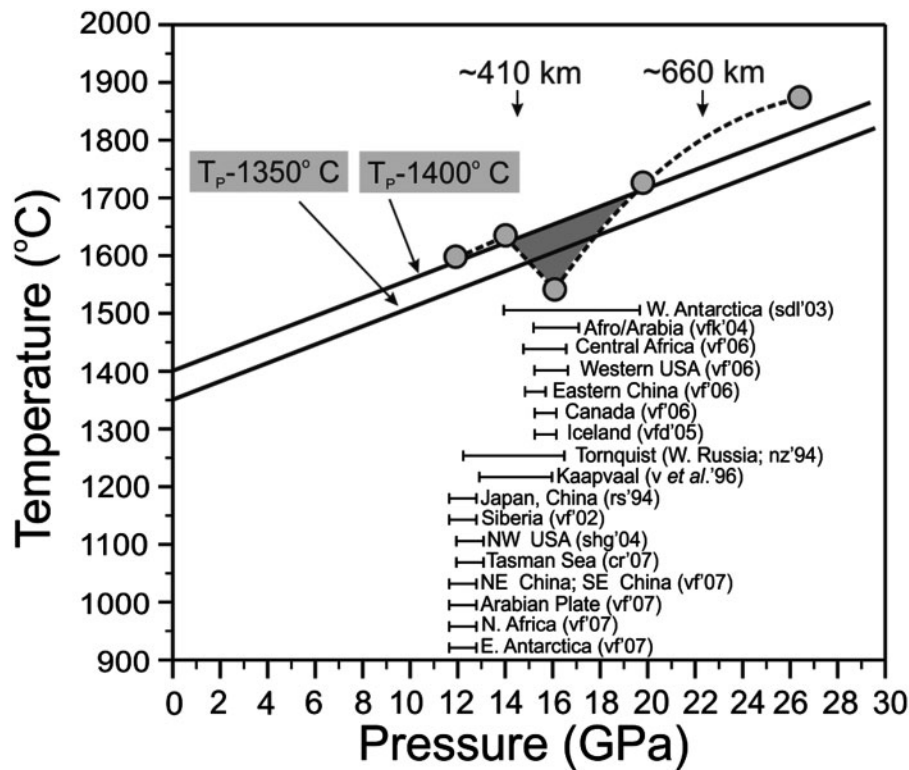


Fig. 14. Seismically detected low-velocity zones (LVZ) projected onto the solidus of model carbonated peridotite in the system CMS–CO₂ (from Fig. 7). To avoid making the figure too complex, the solidus curve is shown connected with only one grey circle at each pressure. The size of the grey circles across the pressure range indicates solidus temperature bounds at 12, 16, 20, and 26 GPa. Two adiabats for ‘normal’ mantle with a potential temperature (T_p) of 1400 and 1350°C, and a gradient of 13°C GPa⁻¹ (Katsura *et al.*, 2004) are shown. There are two types of low-velocity zones shown in this figure. Some of these low-velocity zones appear to be restricted to a depth range of ~350–600 km, corresponding almost exactly to where the solidus of carbonated peridotite abruptly drops, causing enhanced melting. This zone of enhanced melting is shown as a roughly triangular region shaded in grey. In addition to the low-velocity zones found in the Transition Zone, there are a few others that have been detected at a depth of ~350–370 km. All the low-velocity zones are projections onto this P – T diagram, and hence, have nothing to do with the vertical axis representing temperature. Data sources: sdl’03, Sieminski *et al.* (2003); vfk’04, Vinnik *et al.* (2004); vf’02, Vinnik & Farra (2002); vf’06, Vinnik & Farra (2006); vfd’05, Vinnik *et al.* (2005); nz’94, Nolet & Zielhuis (1994); v *et al.*’96, Vinnik *et al.* (1996); rs’94, Revenaugh & Sipkin (1994); shg’04, Song *et al.* (2004); cr’07, Courtier & Revenaugh (2007); vf’07, Vinnik & Farra (2007).

CONCLUSIONS

The solidus curve of simplified carbonated peridotite in the systems CMS–CO₂ and CMAS–CO₂ has a negative slope between 14 and 16 GPa. Below and above this pressure range, the solidus resumes a positive trajectory in P – T space. In both the studied systems, liquid compositions in equilibrium with the relevant crystalline phase assemblage are highly calcic at 16 and 20 GPa. At 16 GPa, the Ca-number of a particular liquid decreases with increasing temperature; however, the highest temperature liquid is still calcic when compared with those at 10–14 or 26 GPa. At 16 GPa and 1475°C, an isobaric invariant point was located experimentally. At this point, wadsleyite + cpx + anhydrous B + magnesite + melt are the stable assemblage, and the liquid is highly calcic. The melting reaction written for this isobaric invariant point shows that even though anhydrous B has the highest coefficient and plots outside the mantle peridotite composition space,

clinopyroxene is the phase that gives the liquid its calcic nature. Upon melting at this invariant point a lot of wadsleyite is produced and hence the reaction is peritectic in nature. With increasing temperature at 16 GPa, once simplified mantle peridotite becomes stable, calcium-silicate phases contribute the most toward liquid production at the solidus, and therefore, combined with the melting reaction for an experiment with anhydrous B, the calcium-rich nature of liquid generated is partially understood. Similarly, calcium-silicate perovskite also dictates the calcic nature of liquids at 20 GPa. However, in both the studied systems, liquids at 10–14 and 26 GPa resemble magnesiocarbonatites. Therefore, although magnesite seemingly controls the solidus temperatures of carbonated peridotite in the studied pressure range, it has little leverage on the liquid compositions, at least in the 16–20 GPa pressure interval. The shape of the solidus in CMS–CO₂ and CMAS–CO₂ remains as yet unexplained. Given

suitable adiabats, a decrease in solidus temperature between 14 and 16 GPa would cause enhanced melting; such melting might be related to seismically imaged low-velocity zones in the Transition Zone of the Earth.

ACKNOWLEDGEMENTS

The authors thank Don Anderson, Lora Armstrong, Dave Dolejš, Dan Frost, Hans Keppler, Robert Luth, Dave Rubie, Max Tirone, Reidar Trønnes, Lev Vinnik, Nico Walte, and Michael Walter for very useful and helpful discussions related to determination of melting phase relations of carbonated peridotite as presented in this paper. Their comments, at various stages, on this work, are noted and are much appreciated. The first author is particularly grateful to Max Tirone for discussions, insights, and explanations pertaining not only to the role that carbonated mantle melting has in the petrology and geochemistry of the Earth, but also on the influence of the former in geodynamic processes. Stefano Poli and two anonymous referees made incisive comments on this paper. The administrative and technical staff members at Bayerisches Geoinstitut, and Geosciences Montpellier, are warmly acknowledged for their assistance that eventually led the authors to prepare this paper. Executive Editor Marjorie Wilson is thanked for her patience during a prolonged revision.

FUNDING

Bayerisches Geoinstitut, Germany supported this research.

REFERENCES

- Armstrong, L. S., Walter, M. J., Keshav, S., Gudfinnsson, G. H., Bulanova, G., Pickles, J., Lord, O. & Lennie, A. (2007). Ca(Ti,Si)O₃ inclusions in diamonds crystallized from carbonate melts in the Transition Zone: experimental constraints. *Transactions of American Geophysical Union* (Fall Meeting).
- Armstrong, L. S., Tuff, J., Walter, M. J., Lennie, A., Clark, S. & Nakajima, Y. (2008). CaSiO₃-CaTiO₃-MgSiO₃ phase relations from 20–50 GPa and the formation of Ca-perovskite inclusions in ultradeep diamonds. *Transactions of American Geophysical Union* (Fall Meeting).
- Brenker, F., Stachel, T. & Harris, J. W. (2002). Exhumation of lower mantle inclusions in diamond: A TEM investigation of retrograde phase transitions, reactions, and exsolution. *Earth and Planetary Science Letters* **198**, 1–9.
- Brenker, F., Vollmer, C. *et al.* (2007). Carbonates from the lower part of the Transition Zone or even the lower mantle. *Earth and Planetary Science Letters* **260**, 1–9.
- Brey, G. P., Brice, W. R., Ellis, D. J., Green, D. H., Harris, K. L. & Ryabchikov, I. D. (1983). Pyroxene-carbonate reactions in the upper mantle. *Earth and Planetary Science Letters* **62**, 63–74.
- Buob, A., Luth, R. W., Schmidt, M. W. & Ulmer, P. (2006). Experiments on CaCO₃-MgCO₃ solid solution at high pressure and temperature. *American Mineralogist* **91**, 435–440.
- Canil, D. (1994). Stability of clinopyroxene at pressure-temperature conditions of the transition region. *Physics of the Earth and Planetary Interiors* **86**, 25–34.
- Canil, D. & Scarfe, C. (1990). Phase relations in peridotite + CO₂ system to 12 GPa: implications for kimberlites and carbonate stability in the Earth's upper mantle. *Journal of Geophysical Research* **95**, 15805–15816.
- Clague, D. A., Paduan, J. B. & Davis, A. C. (2009). Widespread strombolian eruptions of mid-ocean ridge basalt. *Journal of Volcanology and Geothermal Research* **180**, 171–188.
- Courtier, A. M. & Revenaugh, J. (2007). Deep upper mantle melting beneath the Tasman and Coral seas detected with multiple ScS reverberations. *Earth and Planetary Science Letters* **259**, 66–76.
- Dalton, J. A. & Presnall, D. C. (1998). Carbonatitic melts along the solidus of model lherzolite in the system CaO-MgO-Al₂O₃-SiO₂-CO₂. *Contributions to Mineralogy and Petrology* **131**, 123–135.
- Dixon, J. E., Clague, D. A., Cousens, B., Monsalve, M. L. & Uhl, J. (2008). Carbonatite and silicate melt metasomatism of the mantle surrounding the Hawaiian plume: evidence from volatiles, trace elements, and radiogenic isotopes in rejuvenated-stage lavas from Niihau, Hawaii. *Geochemistry, Geophysics, Geosystems* **9**, doi:10.1029/2008GC002076.
- Eggler, D. H. (1976). Does CO₂ cause partial melting in the low-velocity layer of the mantle? *Geology* **4**, 69–72.
- Falloon, T. J. & Green, D. H. (1989). The solidus of carbonated, fertile peridotite. *Earth and Planetary Science Letters* **94**, 364–370.
- Fei, Y. & Bertka, C. (1999). Phase transition in the Earth's mantle and mantle mineralogy. In: Fei, Y., Bertka, C. & Mysen, B. O. (eds) *Mantle Petrology: Field Observations and High-pressure Experimentation*. *Geochemical Society Special Publication* **6**, 189–208.
- Frost, D. J., Langenhorst, F. & van Aken, P. A. (2001). Fe-Mg partitioning between ringwoodite and magnesiowüstite and the effect of pressure, temperature, and oxygen fugacity. *Physics and Chemistry of Minerals* **28**, 455–470.
- Ghosh, S., Ohtani, E., Litasov, K. D. & Terasaki, H. (2009). Solidus of carbonated peridotite from 10 to 20 GPa and the origin of magnesio-carbonatite melt in the Earth's deep mantle. *Chemical Geology* **262**, 17–28.
- Grassi, D. & Schmidt, M. W. (2011). The melting of carbonated pelites from 70 to 700 km depth. *Journal of Petrology* **52**, 765–789.
- Gudfinnsson, G. H. & Presnall, D. C. (2005). Continuous gradations among primary carbonatitic, kimberlitic, melilitic, basaltic, picritic, and komatiitic melts in equilibrium with garnet lherzolite at 3–8 GPa. *Journal of Petrology* **46**, 1645–1659.
- Gudfinnsson, G. H., Keshav, S. & Presnall, D. C. (2007). Melting of hydrous, carbonated mantle peridotite. *Transactions of the American Geophysical Union* (Fall Meeting).
- Gudfinnsson, G. H., Keshav, S. & Presnall, D. C. (2008). Water-rich carbonatites at low pressures and kimberlites at high pressures. *Transactions of the American Geophysical Union* (Fall Meeting).
- Hauri, E. H., Shimizu, N., Dieu, J. J. & Hart, S. R. (1993). Evidence for hot-spot related carbonatite metasomatism in the oceanic upper mantle. *Nature* **365**, 221–227.
- Herzberg, C. & Gasparik, T. (1989). Melting experiments on chondrites at high pressures: stability of anhydrous phase B. *Transactions of the American Geophysical Union* **70**, 484.
- Hirschmann, M. M. & Dasgupta, R. (2007). A modified iterative sandwich method for determination of near-solidus partial melt compositions. I. Theoretical considerations. *Contributions to Mineralogy and Petrology* **154**, 635–645.
- Ito, E. & Takahashi, E. (1987). Melting of peridotite at uppermost lower mantle conditions. *Nature* **328**, 514–517.

- Kaminsky, F. V., Zakharchenko, O. D., Davies, R., Griffin, W. L., Khachatryan-Blinova, G. K. & Shiryaev, A. A. (2001). Super-deep diamonds from the Juina area, Mato Grosso State, Brazil. *Contributions to Mineralogy and Petrology* **140**, 734–753.
- Kato, T. & Kumazawa, M. (1986a). Melting and phase relations in the system $\text{Mg}_2\text{SiO}_4\text{--MgSiO}_3$ at 20 GPa under hydrous conditions. *Journal of Geophysical Research* **91**, 9351–9355.
- Kato, T. & Kumazawa, M. (1986b). Melting experiment on natural lherzolite at 20 GPa: formation of phase B coexisting with garnet. *Geophysical Research Letters* **13**, 181–184.
- Katsura, T. & Ito, E. (1990). Melting and subsolidus relations in the $\text{MgSiO}_3\text{--MgCO}_3$ system at high pressures: implications to evolution of the Earth's atmosphere. *Earth and Planetary Science Letters* **99**, 110–117.
- Katsura, T., Yamada, H. *et al.* (2004). Olivine–wadsleyite transition in the system $(\text{Mg,Fe})_2\text{SiO}_4$. *Journal of Geophysical Research* **109**, doi:10.1029/2003JB002438.
- Keppeler, H. & Frost, D. J. (2005). Introduction to minerals under extreme conditions. In: Miletich, R. (ed.) *EMU Notes in Mineralogy*, 7. Budapest: Eötvös University Press, pp. 1–30.
- Keshav, S. & Gudfinnsson, G. H. (2009). Absence of singularity at the wet solidus of carbonated peridotite. *Transactions of the American Geophysical Union* (Fall Meeting).
- Keshav, S. & Sen, G. (2003). A rare composite xenolith from Salt Lake Crater, Oahu: high-pressure fractionation and implications for kimberlitic melts in the Hawaiian mantle. *Contributions to Mineralogy and Petrology* **144**, 548–558.
- Keshav, S., Corgne, A., Gudfinnsson, G. H., Bizimis, M., McDonough, W. & Fei, Y. (2005). Kimberlite petrogenesis: insights from clinopyroxene–melt partitioning experiments at 6 GPa in the $\text{CaO--MgO--Al}_2\text{O}_3\text{--SiO}_2\text{--CO}_2$ system. *Geochimica et Cosmochimica Acta* **69**, 2829–2845.
- Keshav, S., Gudfinnsson, G. H. & Presnall, D. C. (2006). Majoritic garnets and clinopyroxene in cratonic diamonds: precipitates from CO_2 -rich melts. *European Mineralogy, Petrology, Geochemistry, Bristol*.
- Klein-BenDavid, O., Izraeli, E., Hauri, E. H. & Navon, O. (2004). Mantle fluid evolution—tale of one diamond. *Lithos* **77**, 243–253.
- Klein-BenDavid, O., Wirth, R. & Navon, O. (2006). TEM imaging and analysis of micro-inclusions in diamonds: A close look at diamond-bearing fluids. *American Mineralogist* **91**, 353–365.
- Klein-BenDavid, O., Izraeli, E., Hauri, E. H. & Navon, O. (2007). Fluid inclusions in diamonds from the Diavik Mine, Canada and the evolution of diamond-bearing fluids. *Geochimica et Cosmochimica Acta* **71**, 723–744.
- Litasov, K. D. & Ohtani, E. (2009). Solidus and phase relations of carbonated peridotite in the system $\text{CaO--Al}_2\text{O}_3\text{--MgO--SiO}_2\text{--Na}_2\text{O--CO}_2$ to the lower mantle depths. *Physics of the Earth and Planetary Interiors* **177**, 46–58.
- Liu, L.-G. & Ringwood, A. E. (1975). Synthesis of a perovskite-type polymorph of CaSiO_3 . *Earth and Planetary Science Letters* **28**, 209–211.
- Luth, R. W. (1999). Carbon and carbonates in the mantle. In: Fei, Y., Bertka, C. & Mysen, B. O. (eds) *Mantle Petrology: Field Observations and High-pressure Experimentation, A Tribute to F. R. (Joe) Boyd*. *Geochemical Society Special Publication* **6**, 297–316.
- Luth, R. W. (2006). Experimental study of the $\text{CaMgSi}_2\text{O}_6\text{--CO}_2$ system at 3–8 GPa. *Contributions to Mineralogy and Petrology* **151**, 141–157.
- Luth, R. W. (2009). Melting of carbonated eclogites. *Goldschmidt Conference*. Davos, Switzerland.
- McKenzie, D. P. (1984). The extraction of magma from the crust and upper mantle. *Earth and Planetary Science Letters* **74**, 81–91.
- Minarik, W. G. & Watson, E. B. (1995). Interconnectivity of carbonate melt at low melt fraction. *Earth and Planetary Science Letters* **133**, 423–437.
- Moore, K. R. & Wood, B. J. (1998). The transition from carbonate to silicate melts in the system $\text{CaO--MgO--SiO}_2\text{--CO}_2$. *Journal of Petrology* **39**, 1943–1951.
- Nolet, G. & Zielhuis, A. (1994). Low S velocities under the Tornquist–Teisseyre zone: evidence for water injection into the Transition Zone through subduction. *Journal of Geophysical Research* **99**, 15813–15820.
- Pearson, D. G., Canil, D. & Shirey, S. B. (2003). Mantle samples included in volcanic rocks: xenoliths and diamonds. *Treatise on Geochemistry* **2**, 171–275.
- Presnall, D. C. & Gasparik, T. (1990). Melting of enstatite (MgSiO_3) from 10 to 16.5 GPa and the forsterite (Mg_2SiO_4)–majorite (MgSiO_3) eutectic at 16.5 GPa: implications for the origin of the mantle. *Journal of Geophysical Research* **95**, 15771–15777.
- Presnall, D. C. & Gudfinnsson, G. H. (2005). Carbonate-rich melts in the oceanic low velocity zone and deep mantle. In: Foulger, G. R., Natland, J., Presnall, D. C. & Anderson, D. L. (eds) *Plates, Plumes, and Paradigms*. *Geological Society of America, Special Papers* **388**, 207–216.
- Presnall, D. C. & Gudfinnsson, G. H. (2008). Origin of the oceanic lithosphere. *Journal of Petrology* **49**, 615–632.
- Presnall, D. C. & Walter, M. J. (1993). Melting of forsterite, Mg_2SiO_4 , from 9.7 to 16.5 GPa. *Journal of Geophysical Research* **98**, 19777–19883.
- Presnall, D. C., Weng, Y.-H., Milholland, C. & Walter, M. J. (1998). Liquidus phase relations in the system MgO--MgSiO_3 at pressures up to 25 GPa—constraints on crystallization of a Hadean magma ocean. *Physics of the Earth and Planetary Interiors* **107**, 83–95.
- Presnall, D. C., Gudfinnsson, G. H. & Walter, M. J. (2002). Generation of mid-ocean ridge basalts from 1 to 7 GPa. *Geochimica et Cosmochimica Acta* **66**, 2073–2090.
- Revenaugh, J. & Sipkin, S. (1994). Seismic evidence for silicate melt atop the 410 km mantle discontinuity. *Nature* **369**, 474–476.
- Rohrbach, A. & Schmidt, M. W. (2011). Redox freezing and melting in the Earth's deep mantle resulting from carbon–iron redox coupling. *Nature* **472**, 209–212.
- Schrauder, M. & Navon, O. (1994). Hydrous and carbonatitic mantle fluids in diamonds from Jwaneng, Botswana. *Geochimica et Cosmochimica Acta* **58**, 761–771.
- Schrauder, M., Koeberl, C. & Navon, O. (1996). Trace element analyses of fluid-bearing diamonds from Jwaneng, Botswana. *Geochimica et Cosmochimica Acta* **60**, 4711–4724.
- Shimizu, N. & Sobolev, N. V. (1995). Young peridotitic diamonds from the Mir kimberlite pipe. *Nature* **375**, 394–397.
- Sieminski, A., Debayle, E. & Leveque, J.-J. (2003). Seismic evidence for deep low-velocity anomalies in the transition zone beneath west Antarctica. *Earth and Planetary Science Letters* **216**, 645–661.
- Sisson, T. W., Hankins, W. B. & Presnall, D. C. (1997). Melting of amphibole lherzolite investigated in the system $\text{CMASN--H}_2\text{O--K}_2\text{O}$. *Transactions of American Geophysical Union* (Fall Meeting).
- Sisson, T. W., Kimura, J.-I. & Coombs, M. (2009). Basanite–nephelinite suite from early Kilauea carbonated melts of phlogopite–garnet peridotite at Hawaii's leading magmatic edge. *Contributions to Mineralogy and Petrology* **158**, 803–829.
- Sohn, R. A., Willis, C. *et al.* (2008). Explosive volcanism on the slow-spreading Gakkel Ridge, Arctic Ocean. *Nature* **453**, 1246–1248.
- Song, T.-R. A., HelMBERGER, D. V. & Grand, S. P. (2004). Low-velocity zone atop the 410 km seismic discontinuity in the northwestern United States. *Nature* **427**, 530–533.
- Stachel, T. (2001). Diamonds from the asthenosphere and the Transition Zone. *European Journal of Mineralogy* **13**, 883–892.

- Stachel, T., Harris, J. W., Brey, G. P. & Joswig, W. (2000). Kankan diamonds (Guinea) II: lower mantle inclusion paragenesis. *Contributions to Mineralogy and Petrology* **140**, 16–27.
- Taylor, L. A., Anand, M., Promprated, P., Floss, C. & Sobolev, N. (2003). The significance of mineral inclusions in large diamonds from Yakutia, Russia. *American Mineralogist* **88**, 912–920.
- Tomlinson, E., Jones, A. P. & Harris, J. W. (2006). Co-existing fluid and silicate inclusions in diamonds. *Earth and Planetary Science Letters* **250**, 581–595.
- Tomlinson, E., Mueller, W. & Edinburgh Ion Microprobe Facility (2009). A snapshot mantle metasomatism: trace-element analysis of coexisting fluid (LA-ICMP-MS) and silicate (SIMS) inclusions in fibrous diamonds. *Earth and Planetary Science Letters* **279**, 362–372.
- Vinnik, L. & Farra, V. (2002). Subcratonic low-velocity layer and flood basalts. *Geophysical Research Letters* **29**, doi:10.1029/2001GL014064.
- Vinnik, L. & Farra, V. (2006). S velocity reversal in the mantle Transition Zone. *Geophysical Research Letters* **33**, L18316.
- Vinnik, L. & Farra, V. (2007). Low S velocity atop the 410-km discontinuity and mantle plumes. *Earth and Planetary Science Letters* **262**, 398–412.
- Vinnik, L., Farra, V. & Kind, R. (2004). Deep structure of the Afro-Arabian hotspot by S receiver functions. *Geophysical Research Letters* **31**, L11608.
- Vinnik, L., Foulger, G. L. & Du, Z. (2005). Seismic boundaries in the mantle beneath Iceland: a new constraint on temperature. *Geophysical Journal International* **160**, 533–538.
- Vinnik, L., Green, R. W. E., Nicolaysen, L. O., Kosarev, G. L. & Petersen, N. V. (1996). Deep seismic structure of the Kaapvaal craton. *Tectonophysics* **262**, 67–75.
- Wallace, M. E. & Green, D. H. (1988). An experimental determination of primary carbonatite magma composition. *Nature* **335**, 343–346.
- Walter, M. J., Nakamura, E., Tronnes, R. & Frost, D. J. (2004). Experimental constraints on crystallization differentiation in a deep magma ocean. *Geochimica et Cosmochimica Acta* **68**, 4267–4284.
- Walter, M. J., Bulanova, G. P. *et al.* (2008). Primary carbonatitic melts from subducted oceanic crust. *Nature* **454**, 622–625.
- Walter, M. J. & Presnall, D.-C. (1994). Melting behaviour of simplified lherzolite in the system CaO-MgO-Al₂O₃-SiO₂-Na₂O from 7 to 35 kbar. *Journal of Petrology* **35**, 329–359.
- Wyllie, P. J. & Lee, W.-J. (1998). Model system controls on conditions for formation of magnesiocarbonatite and calciocarbonatite magmas from the mantle. *Journal of Petrology* **39**, 1885–1893.